Available online at www.sciencedirect.com

ScienceDirect

Geochimica et Cosmochimica Acta 292 (2021) 217–234

Geochimica et Cosmochimica Acta

www.elsevier.com/locate/gca

Drivers of zirconium isotope fractionation in Zr-bearing phases and melts: The roles of vibrational, nuclear field shift and diffusive effects

Merlin Méheut [a,*], Mauricio Ibañez-Mejia [b], François L.H. Tissot [c]

[a] Géosciences Environnement Toulouse, CNRS-UPS-OMP, 14 av. Édouard Belin, 31400 Toulouse, France
[b] Department of Earth and Environmental Sciences, University of Rochester, Rochester, NY 14627, USA
[c] The Isotoparium, Division of the Geological and Planetary Sciences, California Institute of Technology, Pasadena, CA 91125, USA

Received 5 June 2020; accepted in revised form 22 September 2020; Available online 1 October 2020

Abstract

Conflicting results exist regarding the mechanisms, direction, and magnitude of Zr isotope fractionation in igneous systems. To better understand the origin of the fractionations observed in magmatic Zr-bearing minerals and bulk rocks, we theoretically investigated the main potential driving processes: thermodynamic equilibrium effects driven by either (i) vibrational energy or (ii) nuclear volume, and (iii) diffusion-driven kinetic effects. Vibrational equilibrium fractionation properties were estimated for zircon ($^{VIII}ZrSiO_4$), baddeleyite ($^{VII}ZrO_2$), gittinsite ($^{VI}ZrCaSi_2O_7$), sabinaite (Na_4 $^{VIII}Zr_2TiC_4O_{16}$), and vlasovite (Na_2 $^{VI}ZrSi_4O_{11}$). These properties show dependency on Zr coordination, as well as the presence of strong covalent bonds (C—O, Si—O by order of decreasing effect) in the material. More importantly, despite the large variety of structures investigated, the predicted mass-dependent equilibrium fractionations ($\Delta^{94/90}Zr$ $\sim\pm0.05$‰ relative to zircon at 800 °C) are systematically one order of magnitude smaller than required to explain the natural variability observed to date in natural settings ($\delta^{94/90}Zr$ from $\sim+1$ to -5‰). Likewise, careful evaluation of expected nuclear field shift (NFS) effects predict a magnitude of fractionation of ~0.08‰ (at 800 °C), further supporting the conclusion that equilibrium effects cannot be invoked to explain extreme $\delta^{94/90}Zr$ zircon values. Furthermore, the mass-dependency of all Zr isotope ratios reported in zircon crystals precludes a contribution of NFS effects larger than ~0.01‰ on $\delta^{94/90}Zr$. On the other hand, we show that diffusion, and in particular the development of Zr diffusive boundary layers in silicate magmas during fractional crystallization, provides a viable and most likely mechanism to produce permil-level, mass-dependent isotope fractionations similar to those observed in natural systems. We propose testable scenarii to explain the large and contrasting Zr isotopes signatures in different magmatic zircons, which underline the importance of magmatic composition, Zr diffusivity, and crystallization timescales.
© 2020 Elsevier Ltd. All rights reserved.

Keywords: Zr isotopes; Zircon; Isotopic fractionation; Diffusion; Nuclear field shift

1. INTRODUCTION

Zirconium isotopes have long been studied in extraterrestrial materials as they hold clues to the chronology of, and stellar contributions to, the early Solar System (*e.g.*, Yin et al., 2000; Akram and Schönbächler, 2016). Recently, investigations of mass-dependent isotopic effects in igneous samples have revealed significant $\delta^{94/90}Zr$ (*i.e.*, $[(^{94}Zr/^{90}Zr_{Sample}/^{94}Zr/^{90}Zr_{Standard}) - 1] * 10^3$) variability at both the mineral (Ibañez-Mejia and Tissot, 2019; Zhang et al., 2019; Guo et al., 2020) and bulk-rock scales (Inglis et al., 2019; Feng et al., 2020; Tian et al., 2020),

* Corresponding author.
E-mail address: merlin.meheut@get.omp.eu (M. Méheut).

https://doi.org/10.1016/j.gca.2020.09.028
0016-7037/© 2020 Elsevier Ltd. All rights reserved.

suggesting Zr isotopes may be useful tracers of magmatic differentiation. Yet, the mechanism(s) driving the observed variability and their petrogenetic significance remain poorly understood. In particular, the direction and magnitude of equilibrium Zr stable isotope fractionation between Zr-bearing phases and silicate melts is unknown.

At thermodynamic equilibrium, heavy isotopes typically populate shorter and stiffer bonds with the lowest coordination number (Schauble, 2004; Young et al., 2015; Blanchard et al., 2017). Since Zr coordination in the melt (*i.e.*, coordination number VI) is expected to be lower than in baddeleyite (VII) or zircon (VIII) (Farges et al., 1991; Louvel et al., 2013), the first-order expectation is that these common Zr-rich phases would be isotopically light relative to the melt from which they crystallize. Such a scenario has recently been invoked by Inglis et al. (2019) to explain a positive correlation between $\delta^{94/90}$Zr and SiO_2 wt.% in bulk volcanic rock samples from the Hekla Volcano, Iceland. In stark contrast, a detailed investigation (Ibañez-Mejia and Tissot, 2019) of single zircon and baddeleyite crystals from a well-characterized gabbroic igneous cumulate (FC-1 anorthositic gabbro from the Duluth Complex, USA) revealed that these Zr-rich phases are isotopically heavy (by up to ~1‰) relative to the starting melt composition (as represented by the bulk rock value). Adding to this conundrum, microbeam (Kirkpatrick et al., 2019; Zhang et al., 2019) and solution (Tompkins et al., 2020) $\delta^{94/90}$Zr data in zircon from several reference localities (*e.g.*, Mud Tank, 91500) display homogeneous compositions, which is at odds with isotope fractionation as being driven by zircon crystallization. Recent LA-ICPMS data by Guo et al. (2020) further complicate the picture, reporting lighter composition in the core (compared to the rims) of zircon from the Gangdese Arc in Tibet, which the authors interpreted as indicative of negative and variable equilibrium fractionation factors between zircon and melt (from −0.12 to −0.45‰).

Here, we approach these conflicting observations from a theoretical standpoint. (i) We performed first-principles, *ab initio* calculations to quantify the direction and magnitude of Zr isotope fractionation between silicate melts and Zr-rich phases at thermodynamic equilibrium. (ii) We explored the potential of Nuclear Field Shift effects for driving significant $\delta^{94/90}$Zr variations, and established a maximum allowable contribution of this effect to the published data. (iii) We evaluated the potential for diffusion-driven (*i.e.*, kinetic) effects as drivers of Zr isotope fractionation. Altogether, these investigations place important constraints on the drivers of Zr isotope variability in Zr-bearing phases and liquids at magmatic temperatures, and highlight that diffusion in silicate melts may be the major mechanism of Zr isotopic fractionation.

2. ZIRCONIUM BONDING ENVIRONMENTS IN SILICATE MELTS AND ZR-RICH PHASES

Differences in the local bonding environment of Zr in silicate liquids and co-existing minerals are the main drivers of vibrational equilibrium isotope fractionation. The speciation of Zr in fluids at high-P-T and in variably hydrated silicate melts of different compositions is fairly well known from studies using molecular dynamics, X-ray absorption spectroscopy near-edge structure (XANES), extended X-ray absorption fine structure (EXAFS) and *ab initio* calculations (Farges et al., 1991; Galoisy et al., 1999; Montorsi et al., 2002; Wilke et al., 2012; Louvel et al., 2013; Wang et al., 2020). These studies have found Zr in silicate melts to exhibit short-range order and to be mainly in octahedral (6-fold) coordination, with six O nearest neighbors and mean Zr-O bond distances ($R_{Zr\text{-}O}$) from 2.05 to 2.13 Å for the first coordination shell. A second shell contribution arises from interactions with tetrahedral-network Si(Na/Al) atoms located at around 3.7 Å (Farges et al., 1991; Farges, 1996, Louvel et al., 2013). Although Zr^{4+} solubility in silicate melts is a strong function of temperature, pressure, and melt composition (Watson, 1979; Watson and Harrison, 1983; Farges et al., 1991; Boehnke et al., 2013; Louvel et al., 2013), experiments at conditions relevant to magmatic environments have found Zr speciation to be independent of temperature and pressure (Louvel et al., 2013), as well as water or halogen (F- and Cl-) contents (Farges et al., 1991; Farges, 1996; Louvel et al., 2013; Wang et al., 2020). Only at high–P-T in fluids with very low Si-Na contents (*i.e.*, <35 wt.%) has Zr^{4+} been observed to occur in 8-fold coordination in a liquid phase (Wilke et al., 2012; Louvel et al., 2013). On the other hand, Zr^{4+} coordination in common Zr-bearing minerals, varies. It is 8-fold in the zircon structure (tetragonal $ZrSiO_4$; Robinson et al., 1971), 7-fold in baddeleyite (monoclinic ZrO_2; Smith and Newkirk, 1965) and can also replace 6-coordinated Ti in Ti-oxide minerals such as ilmenite ($FeTiO_3$) and rutile (TiO_2) (Abrahams and Bernstein, 1971; Farges et al., 1996). Mean $R_{Zr\text{-}O}$ in the first coordination shell of Zr^{4+} are 2.14–2.28 Å for zircon and 2.04–2.18 Å for baddeleyite (Louvel et al., 2013).

In this work, two mineral structures are considered for Zr-bearing phases: zircon (tetragonal $ZrSiO_4$), in which Zr is found in 8-fold coordination, and baddeleyite (monoclinic ZrO_2), where Zr is found in 7-fold coordination (Fig. 1a,b; Robinson et al., 1971; Smith and Newkirk, 1971). To model Zr in the silicate melt, several mineral structures were computed: gittinsite (Fig. 1c; $ZrCaSi_2O_7$), sabinaite (Fig. 1d; $Na_4Zr_2TiC_4O_{16}$), and vlasovite (Fig. 1e; $Na_2ZrSi_4O_{11}$), where Zr is found in, respectively, 6-fold, 8-fold and 6-fold coordination. Vlasovite was chosen here as the best proxy for understanding Zr bonding properties in silicate melts, because Zr^{4+} ions in this structure occupy 6-fold coordinated sites in alkali-zirconosilicate clusters just as those observed in silicate liquids (*e.g.*, Louvel et al., 2013), and Zr-O — bond distances in this phase (ca. 2.09 Å) are similar to those found in silicate liquids (*i.e.*, 2.05–2.13 Å; Farges et al., 1991; Louvel et al., 2013). To more precisely assess the domain of variation of Zr fractionation properties, Zr-bearing minerals of contrasting compositions and Zr bonding characteristics and coordination number, yet representative of magmas, were further considered. Only experimentally resolved and ordered structures, with unit cells sufficiently small to avoid prohibitively difficult computation, were retained. Gittinsite and sabinaite were found to be the best choices for this, among other existing minerals that were considered (*e.g.*,

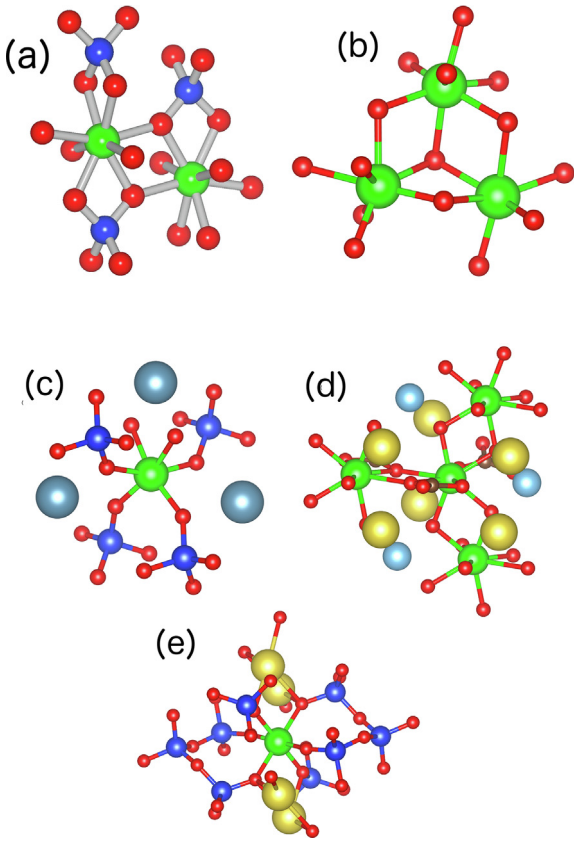

Fig. 1. Mineral structures modeled in this study: (a) zircon $^{VIII}ZrSiO_4$; (b) baddeleyite $^{VII}ZrO_2$; (c) gittinsite $^{VI}ZrCaSi_2O_7$; (d) sabinaite Na_4 $^{VIII}Zr_2TiC_4O_{16}$; (e) vlasovite Na_2 $^{VI}ZrSi_4O_{11}$. Green: Zr atoms; red: oxygen atoms; deep blue: Si atoms; yellow: Na atoms; light blue: Ti atoms; grey blue: Ca atoms. Roman numerals denote coordination number. (For interpretation of the references to colour in this figure legend, the reader is referred to the web version of this article.)

catapleiite $Na_2ZrSi_3O_9.2H_2O$, armstrongite $CaZrSi_6O_{17}H_4$, tumchaite $Na_2(Zr,Sn)Si_4O_{11}.2H_2O$, painite $CaZrBAl_9O_{18}$, elpidite $Na_2ZrSi_6O_{18}H_6$, georgechaoite $NaKZrSi_3O_9.2H_2O$, or calzirtite $Ca_2Zr_5Ti_2O_{16}$).

3. METHODS

The equilibrium fractionation of Zr isotopes between two phases is obtained by combining the β-factors of both phases. The β-factor corresponds to the isotopic fractionation factor between the phase, and a perfect gas of Zr atoms. This quantity can be computed within the harmonic approximation from the vibrational frequencies of the phase of interest (Urey, 1947). If a is a crystalline solid, and Y the element of interest, the β-factor of phase a for the Y/Y* isotopic substitution can be written as:

$$\beta(a,Y) = \left[\frac{Q(AY^*_N)}{Q(AY_N)}\right]^{1/N}\left[\frac{m_Y}{m_{Y^*}}\right]^{3/2} \quad (1)$$

where $Q(AY^*_N)$ is the partition function of the system having all the Y atoms substituted by Y^*. The partition function of a crystalline solid can be estimated from its harmonic phonon frequencies:

$$Q = \left[\prod_{i=1}^{3N^{at}}\prod_{\{\boldsymbol{q}\}}^{*}\frac{e^{-h\nu_{\boldsymbol{q},i}/(2kT)}}{1-e^{-h\nu_{\boldsymbol{q},i}/(kT)}}\right]^{\frac{1}{N_q}} \quad (2)$$

where $\nu_{\boldsymbol{q},i}$ are the frequencies of the phonon with wavevector $\mathbf{q}$ and branch index $i = 1,3N^{at}$. N^{at} is the number of atoms in the unit cell, N is the number of Y atoms in the unit cell, T is the absolute temperature, k is the Boltzman constant and h is Planck's constant. The product is performed on a sufficiently large grid of N_q $\mathbf{q}$-vectors in the Brillouin zone. The * symbol above the product indicates that the three translational modes with $\nu_{\boldsymbol{0},i} = 0$ are not considered.

The phonon frequencies are computed from first principles within density functional theory (DFT) (Hohenberg and Kohn, 1964; Kohn and Sham, 1965), using the local density approximation to the exchange-correlation functional of Perdew and Zünger (PZ) (Perdew and Zunger, 1981). This approach is necessary because the gradient-corrected functionals typically used in previous studies, such as BLYP or PBE (*e.g.*, Dupuis et al., 2015), have been shown inappropriate to describe Zr-containing materials such as the ZrO_2 polymorphs (Fadda et al., 2010a, b). A plane-wave basis set, and atomic pseudopotentials were used. The pseudopotentials for Si and O were generated for the PZ functional using the same characteristics as those described in the electronic annexes of Méheut et al. (2007), which were generated for the PBE functional. The pseudopotentials for Na, Ti, C and Ca are taken from the PSlibrary (Dal Corso, 2014). For Zr, we considered two pseudopotentials. The first one is taken from the PSLibrary and is therefore ultrasoft. This permits a numerically efficient calculation, but the computation of Raman intensities is not implemented for this type of pseudopotentials in the Quantum Espresso software package. In order to compute Raman intensities for baddeleyite and zircon, and compare precisely their calculated gamma-point frequencies with experimental spectra, we generated a Zr norm-conserving pseudopotential (Troullier and Martins, 1991) in the Kleinman–Bylander form (Kleinman and Bylander, 1982), similar to the ones used for O and Si. For this second Zr pseudopotential, hereafter referred to as "Zrtm", we used the $4p^6$ $4d^4$ $4s^2$ configuration with core radii of 1.20 a.u. for each orbital and the local potential is s. For the computations of all the minerals not using the Zrtm pseudopotential, electronic wave-functions are expanded in plane-waves up to an energy cutoff $\varepsilon cut = 80$ Ry and the charge density cut-off is set to 4 εcut. For the calculations of zircon and baddeleyite using Zrtm, electronic wave-functions are expanded in plane-waves up to an energy cutoff $\varepsilon cut = 200$ Ry and the charge density cut-off is set to 4 εcut. Electronic integration is done by sampling the Brillouin zone with a $3 \times 3 \times 3$k-point grid for zircon, baddeleyite and gittinsite, a $3 \times 1 \times 3$ grid for sabinaite and a $2 \times 2 \times 2$ grid for vlasovite (Monkhorst and Pack, 1976).

Phonon frequencies were computed using linear response theory (Baroni et al., 2001), with the Quantum-Espresso package (Giannozzi et al., 2009). Interatomic

force-constants are obtained from the dynamical matrices computed exactly (within DFT) on a $n \times n \times n$ grid of q-vectors ($n = 3$ for baddeleyite, zircon, sabinaite, gittinsite, $n = 2$ for vlasovite). Long-range effects are taken into account by computing Born effective-charges and static dielectric constants (Baroni et al., 2001). Dynamical matrices and thus phonon frequencies, can then be obtained in any point of the reciprocal space by Fourier-interpolation of the force constants. For all materials, the vibrational partition function is converged with a $6 \times 6 \times 6$ interpolation grid. In order to help correlate calculated frequencies at gamma-point with experimental spectroscopic (Raman or infrared (IR)) data, we computed the intensities (IR or Raman cross-sections). IR cross-sections were computed for all the modes whereas Raman cross-sections can only be computed for the Zrtm calculation. For Raman-active modes, non-resonant Raman cross-sections were computed using second-order response as in Lazzeri and Mauri (2003). For IR-active modes, cross-sections were computed from the Born effective charges and static dielectric constant (see Balan et al., 2001 for a more detailed description). Note that we used these intensities in a rather qualitative way, in order to distinguish between "important" and weak modes. A proper modeling of IR or Raman spectra would require treatment of polarization, medium and particle shape effects (for IR: Balan et al., 2001; for Raman: Lazzeri and Mauri, 2003), which is beyond the scope of the present study.

4. RESULTS

4.1. Structure and vibrational properties

The equilibrium computed structures of the new materials considered in this study are reported in Table 1 and compared with experimental data. In all cases, atomic positions and cell parameters are obtained after relaxation at zero pressure, until the residual forces are less than 10^{-3} Ry/Å (10^{-12} N). Except for the c-axis of sabinaite, all cell parameters of the relaxed structures underestimate experimental values by 0.5–1.5%. These calculated structural parameters are further compared with selected previous theoretical studies, representative of the range of values obtained for calculations made with the same functional (Local Density Approximation (LDA), Table 1). In both cases, our calculations fall within the range of previous results. For baddeleyite, we refer to the detailed discussion of Fadda et al., 2009 for comparison with other studies.

In the case of sabinaite, the c-axis length is underestimated by 2.3%. Sabinaite structure consists of (Zr,Ti)O layers alternating with $NaCO_3$ layers. While Zr-O distances are normally underestimated by the calculation (within 0.5–1.5%), we note that Na-Na distances are more notably underestimated (by 3.9%). Similarly, calculation of calcite structure within LDA results in c-axis lengths (and therefore Ca-Ca distances) are underestimated by 3.7% (*e.g.*, Valenzano et al., 2006). The unusual discrepancy with respect to the experimental data available for sabinaite is therefore interpreted as a failure of LDA to treat cation-CO_3^{2-} bonds consistently with other bonds. Although this observation implies that the sabinaite calculations should be taken with more caution than those from other phases, the obtained result is useful because it informs on the effect that a change in the chemical environment of Zr might have on its fractionation properties.

The computed phonon frequencies of baddeleyite and zircon at the zone center (wave vector = 0) are compared with spectroscopic measurements in Table 2 (Raman data) and Table 3 (IR data), and illustrated in Fig. 2. All calculated mode frequencies, along with IR and Raman

Table 1
Lattice parameters and selected structural parameters of baddeleyite, zircon, sabinaite, vlasovite and gittinsite, compared with experiments (Exp).

	Cell parameter	LDA (this work)	LDA Zrtm (this work)	Exp	Litterature LDA	
Baddeleyite	*a*(Å)	5.1081 [−0.8%]	5.1075 [−0.8%]	5.1505(1)[a]	5.180[f]	5.108[g]
	b(Å)	5.1849 [−0.5%]	5.1770 [−0.7%]	5.2116(1)[a]	5.231[f]	5.170[g]
	c(Å)	5.2691 [−0.9%]	5.2729 [−0.8%]	5.3173(1)[a]	5.370[f]	5.272[g]
	β	99.696	99.730	99.230[a]	99.61[f]	99.21[g]
Zircon	*a*(Å)	6.5684 [−0.5%]	6.5650 [−0.6%]	6.6042(4)[b]	6.54[h]	6.551[i]
	c(Å)	5.9303 [−0.8%]	5.9293 [−0.8%]	5.9796(3)[b]	5.92[h]	5.940[i]
Sabinaite	*a*(Å)	10.0950 [−1%]		10.196(1)[c]		
	b(Å)	6.5725 [−0.7%]		6.616(1)[c]		
	c(Å)	17.5494 [−2.3%]		17.958(3)[c]		
	β	94.47		94.14[c]		
Vlasovite	*a*(Å)	10.9518 [−0.8%]		11.0390(5)[d]		
	b(Å)	10.0393 [−0.6%]		10.0980(3)[d]		
	c(Å)	8.5172 [−0.6%]		8.5677(4)[d]		
	β	100.605				
Gittinsite	*a*(Å)	6.7624 [−1.3%]		6.852(2)[e]		
	b(Å)	8.5947 [−0.7%]		8.659(1)[e]		
	c(Å)	4.6540 [−0.7%]		4.686(2)[e]		
	β	101.50		101.69[e]		

Numbers in parenthesis, (), refer to uncertainties on the last significant digit. Numbers in square brackets, [], refer to the % difference between the calculated and experimental values. 'Zrtm' refers to calculations done with a different Zr pseudopotential (see Methods).
References: a: Howard et al. (1988); b: Hazen and Finger (1979); c: McDonald (1996); d: Sokolova et al. (2006); e: Roelofsen-Ahl and Peterson (1989); f: Fadda et al. (2009), TM calculation of Table IV; g: Zhao and Vanderbilt (2002); h: Rignanese et al. (2001); i: Qin et al. (2016).

Table 2
Comparison of model and measured Raman phonon frequencies in Baddeleyite and Zircon.

	LDA[a] (cm^{-1})	Int[b]	Exp[c] (cm^{-1})		LDA[a] (cm^{-1})	Int[b]	Exp[c] (cm^{-1})
Baddeleyite							
A_g	103.43	6	101	B_g	177.29	6	na
A_g	183.29	13	177	B_g	227.49	6	222.5
A_g	190.79	17	189.5	B_g	315.96	2	na
A_g	319.92	37	310.5[§]	B_g	335.84	30	331.6
A_g	349.61	23	348.1	B_g	388.08	46	378
A_g	386.31	17	384.9	B_g	495.18	24	501.1
A_g	473.96	180	474.1	B_g	537.47	32	537.5
A_g	552.48	53	556.3	B_g	607.39	102	614.4
A_g	638.66	145	635.0	B_g	754.83	22	745[§§]
Zircon							
A_{1g}	437	59	439	B_{2g}	257	0.5	266
A_{1g}	960	25	974	E_g	195	2	202
B_{1g}	224	3	215	E_g	225	3	225
B_{1g}	390	3	393	E_g	362	24	356
B_{1g}	626	1	641	E_g	535	0.1	546
B_{1g}	1005	251	1008	E_g	914	0.02	923

[a] LDA refers to the present calculation.
[b] Int.: calculated Raman cross-section in atomic units.
[c] For zircon, measurements (exp) come from Kolesov et al. (2001). For baddeleyite, measurements (exp) correspond to the study of Carlone (1992) at 15 K. Other experimental data at 300 K, when different by more than 5 cm^{-1}, are listed below.
[§] The peak at 310.5 cm^{-1} measured at 15 K by Carlone (1992) is found at 305 cm^{-1} at 300 K, by Carlone (1992), Ishigame and Sakurai (1977) and Quintard et al. (2002).
[§§] The peak at 745 cm^{-1} measured at 15 K by Carlone (1992) corresponds to a broad feature difficult to discriminate, and measured at 757 cm^{-1} by Quintard et al. (2002), and 780 cm^{-1} by Carlone (1992), at 300 K.

Table 3
Comparison of model and measured IR phonon frequencies (TO: transversal optic; and LO: longitudinal optic modes[a]) in baddeleyite and zircon.

	LDA[b] (cm^{-1})	Int.[c]	Exp[d] (cm^{-1})		LDA[b] (cm^{-1})	Int.[c]	Exp[d] (cm^{-1})
Baddeleyite	TO-LO		TO		TO-LO		TO
A_u	183	0.1	na	B_u	229–241	16–7	224[§]
A_u	245–246	1	na	B_u	307	1	na
A_u	256–275	16–1	257	B_u	324–359	70–40	324
A_u	353–370	27–1	351	B_u	362–441	54–23	376
A_u	406–464	50–2	420	B_u	418–481	35–28	440
A_u	486–553	20–5	511	B_u	490–663	31–72	511
A_u	580–761	17–125	588	B_u	719–807	19–86	725
A_u	640	0.1	687				
Zircon	TO-LO		TO-LO		TO-LO		TO-LO
A_{2u}	343–473	43–14	338–475	E_u	283–340	26–2	282–351
A_{2u}	596–638	10–14	606–644	E_u	376–416	10–1	385–416
A_{2u}	969–1087	49–73	980–1101	E_u	422–462	1–22	431–470
				E_u	858–1019	61–82	880–1030

[a] See Balan et al. (2001) and ref therein for details.
[b] LDA refers to the present calculation.
[c] Int.: calculated IR cross-section in atomic units.
[d] Measurements (exp) are from Zhang et al. (1999) for baddeleyite and Nasdala et al. (2003) for zircon.
[§] Has been ascribed to the Au symmetry by Zhang et al. (1999).

intensities, are reported and most are assigned to a corresponding mode. Theoretical frequencies show very good agreement with measured ones.

4.2. Fractionation properties

The β-factors for zircon, baddeleyite and the mineral structures representative of Zr in silicate melts are shown in Fig. 3. Predicted equilibrium isotope fractionations between all calculated phases relative to zircon (*i.e.*, calculated from differences in β-factors as $\Delta_{A\text{-}B} \simeq 10^3 \ln\alpha_{A\text{-}B} = 10^3 \ln\beta_A - 10^3 \ln\beta_B$) are shown in Fig. 4. The coefficients of the polynomial expansion of $10^3 \ln\beta$ in terms of even powers of the inverse of temperature (in K): $10^3 \ln\beta = A_1/T^2 + A_2/T^4 + A_3/T^6$, are reported in Table 4, from which the mean force constant, noted <F>

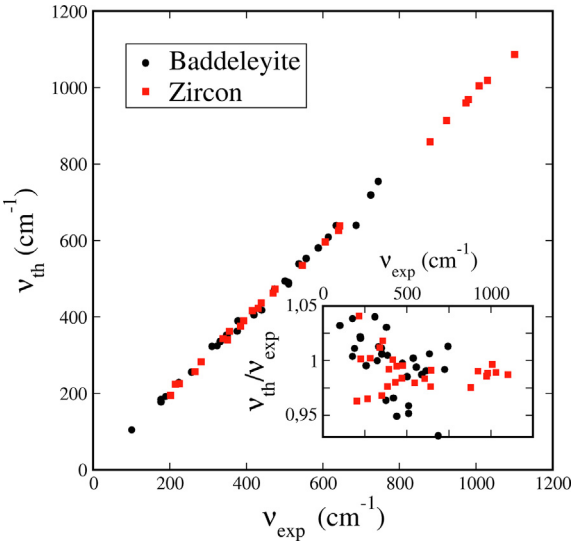

Fig. 2. Comparison of experimental and theoretical vibrational frequencies. Inset: ratio between experimental frequencies and theoretical frequencies.

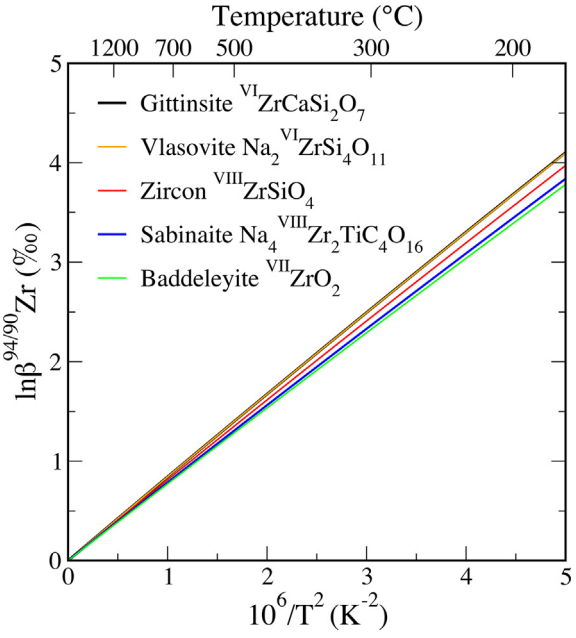

Fig. 3. Temperature dependence of ln β values (in ‰) for $^{94}Zr/^{90}Zr$ in various minerals investigated here. See text for details on calculation methods.

(in N/m), of the chemical bond between Zr and its coordination atoms in each phase, are calculated (see Table 4 footnote for details). For a given phase, at magmatic temperatures, the equilibrium isotope fractionation factor can be easily calculated using the force constant (*e.g.*, Dauphas et al., 2012; Dauphas et al., 2018 and references therein), as:

$$1000\ \ln\beta = \langle F\rangle 1000\left(1/m_{light} - 1/m_{heavy}\right)\hbar^2/\left(8k_B^2T^2\right),$$

where m_{light} and m_{heavy} are the masses of the light and heavy isotopes (in kg), respectively, $\hbar$ is the reduced

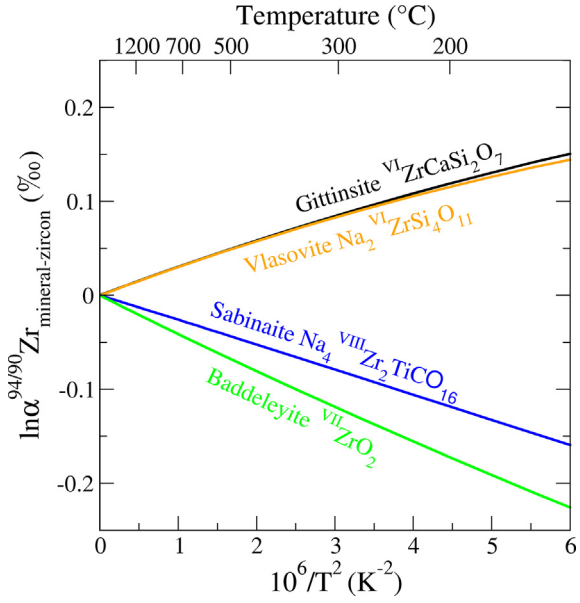

Fig. 4. Temperature dependence of mineral-zircon isotope fractionation factors (1000 ln $\alpha_{mineral\text{-}zircon} \approx \Delta^{94/90}Zr_{mineral\text{-}zircon}$) for $^{94}Zr/^{90}Zr$ for various minerals investigated here.

Table 4
Fits of 10^3 ln $\beta(^{94/90}Zr)_{mineral}$ for 135–1200 °C, based on $A_1x + A_2x^2 + A_3x^3$ with $x = 10^4/T^2$.

Mineral	<F> (N/m)[§]	A_1	A_2	A_3
gittinsite	407.8	84.88	−61.74	99.92
vlasovite	407.8	84.88	−63.52	101.78
zircon	392.7	81.75	−50.39	82.53
sabinaite	380.4	79.18	−53.31	106.62
baddeleyite	372.4	77.53	−41.00	49.53

[§] The mean force constants are calculated using the relationship $A_1 = 1000\ (1/m_{light} - 1/m_{heavy})\ \hbar^2/(8\ k_B^2) \times \langle F\rangle$ (see Dauphas et al., 2012).

Planck's constant (J·s), k_B is Boltzmann's constant (J/K), and T is the absolute temperature. For $^{94}Zr/^{90}Zr$ ratios, this expression reduces to 1000 ln$\beta(^{94/90}Zr) \approx 2081.6\ \langle F\rangle/T^2$.

At thermodynamic equilibrium, heavy isotopes typically populate shorter and stiffer bonds with the lowest coordination number (Schauble, 2004; Young et al., 2015; Blanchard et al., 2017). Consistent with these first-order expectations, vlasovite (VI) and gittinsite (VI) are isotopically indistinguishable from each other (<F> = 407.8 N/m for both phases), and heavier than zircon (VIII) (<F> = 392.7 N/m). On the other hand, baddeleyite (VII) (<F> = 372.4 N/m) and sabinaite (VIII) (<F> = 380.7 N/m) are lighter than zircon (VIII).

In order to better understand why materials with higher coordination can be isotopically heavier (*e.g.*, zircon or sabinaite w/r to baddeleyite), we analyzed the vibrational contributions to fractionation properties for these various materials (methodology described in Méheut et al., 2009). The results, shown in Fig. 5, reveal a complex situation. For zircon and baddeleyite (Fig. 5a), the main contribution

to Zr isotopic fractionation comes from low (typically 100–400 cm^{-1}) frequencies. However, zircon also presents some significant contributions at frequencies higher than baddeleyite. In particular, the contribution of the highest frequencies of zircon (~900 cm^{-1}) is non-negligible (0.08‰ in total). These high frequencies correspond to Si-O— stretching modes. In addition to coordination, this observation suggests the importance of phase chemical composition in influencing Zr isotope fractionation properties, and more specifically of the presence of Si in the structure. The presence of Si in the mineral leads to high frequency modes (Si-O— stretching modes), and, assuming that these would present a non-negligible coupling with Zr displacement, high frequency Zr displacement would occur, leading to high frequency contribution to the β-factor. The two other materials containing Si (gittinsite and vlasovite, Fig. 5c) present a very similar contribution of Si-O stretching modes (~0.08‰ in total). Now, looking at sabinaite (Fig. 5b), which is a carbonate, we can also distinguish a contribution of C-O— stretching frequencies (~1350–1650 cm^{-1}). This contribution is smaller than for Si-O (~0.04‰), which means that the coupling of Zr movement with these displacements might be smaller. Nevertheless, this feature is once again able to explain the heavier isotopic composition of sabinaite with respect to baddeleyite (despite of their respective coordination), as the integrated contribution to the β-factor of sabinaite becomes greater than that of baddeleyite above this spectral domain.

Perhaps more important than the relative isotope fractionation factors is the fact that, at magmatic temperatures, the magnitude of these isotope effects are extremely small. Even at 800 °C, the maximum equilibrium zircon-melt or baddeleyite-melt fractionation is ≤0.05‰. At 1200 °C these effects are ≤0.02–0.03‰.

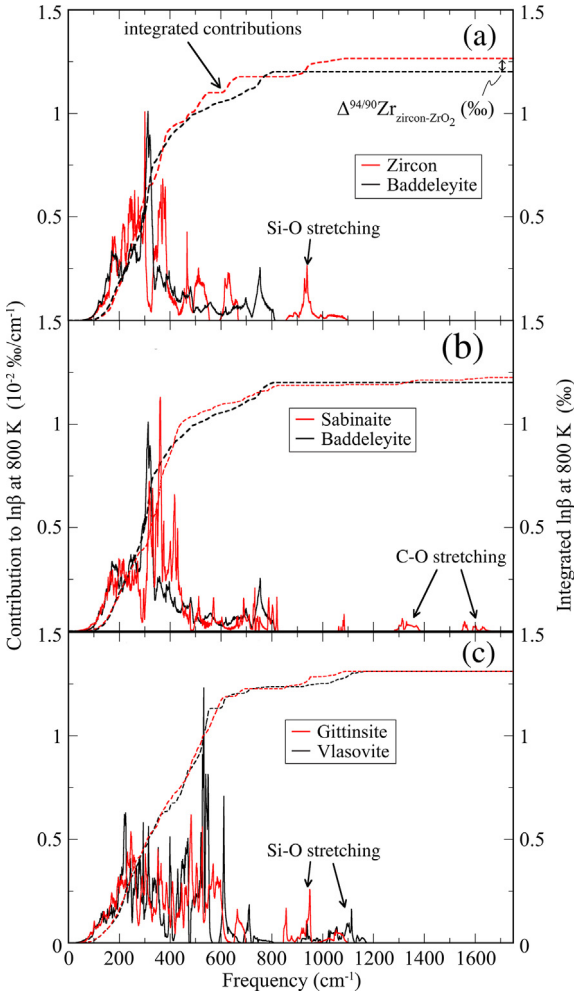

Fig. 5. Comparison of the spectral contributions to the zirconium β-factors of (a) zircon and baddeleyite; (b) sabinaite and baddeleyite; (c) vlasovite and gittinsite.

5. DISCUSSION

5.1. Negligible equilibrium Zr isotope fractionation vs. observed magmatic trends

The results of our *ab initio* calculations indicate that vibrational equilibrium Zr isotope effects can only yield minute zircon-melt Zr isotope fractionation; *i.e.*, $\Delta^{94/90}Zr_{zircon\text{-}melt} = (\delta^{94/90}Zr_{zircon} - \delta^{94/90}Zr_{melt})$ ~0.05‰ at 800 °C. This very limited degree of fractionation is consistent with the inter- and intra-crystal Zr isotope homogeneity observed in some reference zircon localities: *e.g.*, 91500, Mud Tank and Plešovice (LA-ICPMS: Zhang et al., 2019; SIMS: Kirkpatrick et al., 2019; double-spiked solutions: Tompkins et al., 2020).

These small fractionation factors are, however, at least one order of magnitude smaller than those required to explain the data obtained for multiple igneous systems (Fig. 6). Ibañez-Mejia and Tissot (2019) inferred a $\Delta^{94/90}Zr_{zircon\text{-}melt} \approx +1$‰ through direct comparison of $\delta^{94/90}Zr$ values from 70 individual crystals of Zr-rich

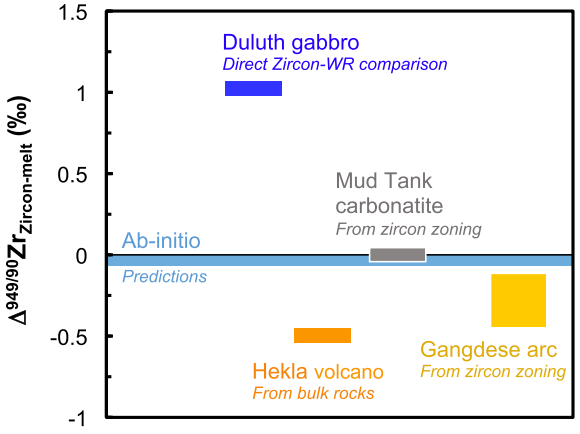

Fig. 6. Comparison of the zircon-melt fractionation factors ($\Delta^{94/90}Zr_{zircon\text{-}melt} = \delta^{94/90}Zr_{zircon} - \delta^{94/90}Zr_{melt}$, in ‰) predicted by *ab initio* calculations at 700 °C (this work) with those derived from the analyses of igneous samples: Duluth gabbro zircons (Ibañez-Mejia and Tissot, 2019), Hekla volcano bulk rocks (Inglis et al., 2019), Mud Tank carbonatite zircon megacryst (Tompkins et al., 2020) and Gangdese arc zircons (Guo et al., 2020). For many of the systems studied, equilibrium mass-dependent effects do not seem to be the main driver of isotopic fractionation.

accessory phases (zircon and baddeleyite) and the bulk rock of a well-characterized gabbroic igneous cumulate (FC-1, Duluth gabbro). Inglis et al., 2019 hypothesized that the positive correlation between $\delta^{94/90}Zr$ and SiO_2 wt.% in bulk volcanic-rock samples from the Hekla Volcano (Iceland) was the result of zircon removal with a $\Delta^{94/90}Zr_{zircon\text{-}melt} \approx -0.50‰$. The variable ($\sim$−0.12 to −0.45‰) fractionation factors reported by Guo et al. (2020) for zircons in the juvenile Gangdese Arc (southern Tibet), come from laser ablation determination of zircon crystal zoning, which revealed lighter compositions towards the core and heavier compositions towards the rims of the crystals. Interpretations regarding the driving mechanisms behind these effects also varied between studies: Inglis et al. (2019) and Guo et al. (2020) attributed these large effects to mass-dependent equilibrium isotope fractionation during Zr crystallization, whereas Ibañez-Mejia and Tissot (2019) highlighted the fact that equilibrium effects may not be the sole driver of these isotope fractionations. The results of the *ab initio* calculations presented here confirm the latter hypothesis, indicating that none of these data can be explained by mass-dependent, vibrational, equilibrium isotope effects. In the next sections, we consider alternative drivers of Zr isotope fractionations.

5.2. Nuclear Field Shifts as drivers of Zr isotope fractionation?

The first-principle calculations presented above quantify mass-dependent isotope fractionations stemming from differences in the vibrational properties of the chemical bonds in Zr isotopologues (Bigeleisen and Mayer, 1947; Urey, 1947), but do not account for the so-called Nuclear Field Shift (NFS) effects, which arise from differences in the volume and shape of atomic nuclei (Bigeleisen, 1996; Knyazev and Myasoedov, 2001; Schauble, 2007; Yang and Liu, 2016). Below, we examine the possibility that NFS could result in significant Zr isotope fractionation at magmatic temperatures.

NFS effects manifest as, and are named after, shifts in the emission/absorption frequencies of isotopic atoms that cannot be explained by mass differences and hyperfine splitting (King, 1984). To first order, they scale proportionally to $|\Psi(0)|^2\ \delta\langle r^2_{Nuc}\rangle$, where $|\Psi(0)|^2$ is the total electron density at the nucleus, and $\delta\langle r^2_{Nuc}\rangle$ is the isotopic change in the mean-square nuclear charge radius (*e.g.*, King, 1984; Schauble, 2007). Because nuclei with odd (or magic) numbers of neutrons, tend to have smaller nuclear charge radii than expected based on simple interpolation between their neighboring isotopes, NFS effects tend to display diagnostic, mostly odd-even staggering, patterns (*e.g.*, Hg isotopes, Bergquist and Blum, 2007). As mass-dependent fractionation decreases with increasing mass, and NFS increase with electron density at the nucleus, NFS effects are most pronounced in heavy elements (*i.e.*, with large nuclei), where they can become the dominant fractionation mechanism (*e.g.*, NFS during U redox reactions are 3x larger than mass-dependent effects, Bigeleisen, 1996; Schauble, 2007; Abe et al., 2008). Furthermore, while mass-dependent fractionation scales proportionally to $1/T^2$, NFS effects scale with 1/T, which implies that their relative contribution to the total isotope fractionation increases in high-T (*e.g.*, igneous) environments.

To determine the magnitude of equilibrium NFS effects, one can either (i) perform *ab initio* calculations that directly model the electronic structures of the nuclei while explicitly varying nuclear charge radii (*e.g.*, Knyazev and Myasoedov, 2001; Schauble, 2007; Abe et al., 2008), or (ii) perform equilibrium exchange reactions and measure the resulting isotopic effects, which can be broken down into mass-dependent and NFS contributions (*e.g.*, Fujii et al., 2009), provided both odd and even isotopes are analyzed. At this time, neither type of data are available for Zr. Nevertheless, some general considerations can be made.

Because electrons in *s*-orbitals can cause larger electron density at the nucleus than *p*-, *d*-, or *f*-orbitals, heavier isotopes will preferentially be enriched in the species with fewer *s* electrons, or more *p*, *d* and *f* electrons (Schauble, 2007). This, for instance, results in ^{238}U enrichments in reduced, U^{4+}-$[Rn]5f^2$, species relative to oxidized, U^{6+}-$[Rn]5f^0$, species, which has led to the development of U isotopes as tracers of redox conditions in the ocean (*e.g.*, Weyer et al., 2008; Tissot and Dauphas, 2015), and possibly in magmatic environments (*e.g.*, Tissot et al., 2019). In all phases considered here, zirconium is present as Zr^{4+}, removing the possibility that NFS effects arise from redox changes and associated differences in the population of electron orbitals. Instead, differences in the electronic structure of the nuclei must therefore mainly be driven by differences in size and shape of the Zr isotope nuclei, and thus changes in the mean-squared nuclear charge radius, $\delta\langle r^2\rangle$. Fig. 7a shows the $\delta\langle r^2\rangle$ of natural Zr isotopes, and Fig. 7b shows $\delta\langle r^2\rangle$ variations normalized to ^{90}Zr and ^{94}Zr. The isotopic patterns for Zr shown in Fig. 7 do not conform to the typical odd–even staggering observed for many other elements (*e.g.*, Mo) for two reasons: (i) ^{90}Zr has a magic number of neutrons ($N = 50$), which means it consists of entirely closed shells of neutrons (King, 1984), resulting in a particularly compact nucleus which removes most of the expected ^{90}Zr-^{91}Zr-^{92}Zr odd–even staggering. (ii) ^{96}Zr has the peculiar property of being doubly-magic (Angeli et al., 2009), with filled subshells of both protons ($Z = 40$) and neutrons ($N = 56$), resulting in a more compact nucleus, making ^{96}Zr deviate from the expected mass-dependent relationship of even isotopes. Because NFS effects scale proportionally to $\delta\langle r^2\rangle$ values, Zr NFS-induced effects, normalized to ^{90}Zr-^{94}Zr, are expected to show significant and opposite anomalies on, respectively, ^{96}Zr and ^{92}Zr (Fig. 7b).

Currently, detection of NFS effects in natural samples is limited to the heaviest elements (*e.g.*, Hg, Tl, U), and calculations of NFS effects for elements in the $\sim$90–100 amu mass range predict only small effects (Knyazev and Myasoedov, 2001; Schauble, 2007). With no available data on the magnitude of NFS effects for Zr isotopes, we use molybdenum (Mo) as a proxy to draw first-order estimates on Zr effects. Molybdenum and Zr are both transition metals, with three isobaric isotopes (92-94-96), and the variations in the root mean-square nuclear charge radii of their isotopes are similar, if only slightly larger for Mo (Fig. 7b). Liquid-liquid isotope exchange experiments

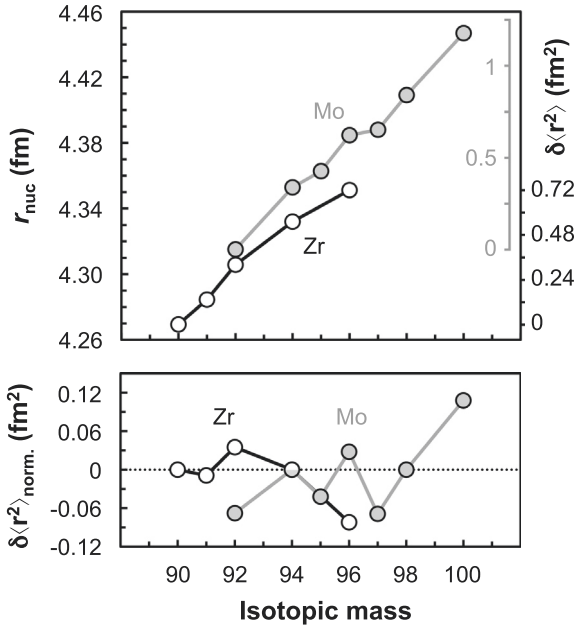

Fig. 7. (a) Root mean-square nuclear charge radii for Zr and Mo isotopes. Secondary axis shows variations of mean-square nuclear charge radii relative to ^{90}Zr (lower axis) and ^{92}Mo (top axis). Uncertainties are smaller than symbols. Data from Angeli and Marinova, 2013. (b) Variations in mean-square nuclear charge radii normalized to ^{90}Zr-^{94}Zr and ^{94}Mo-^{98}Mo, following Fujii et al., (2006a). NFS are expected to present a similar staggered pattern, with the strongest impact on ^{96}Zr.

performed at 295 K (Fujii et al., 2006b) reported isotope fractionation patterns consistent with NFS equilibrium effects of ~0.08‰/amu for Mo. Assuming a simple 1/T temperature dependency, this translates to effects of ~0.02‰/amu at magmatic temperatures of 800–1000 °C. Based on the similar extent of variability of the mean-square nuclear charge radii of Mo and Zr, it is reasonable to expect similar magnitudes of NFS effects for Zr, which would result in a $\delta^{94/90}$Zr of ~0.08‰ at magmatic temperatures. While 2 to 3x larger than the – vibrational – equilibrium mass-dependent effects we predict (Fig. 4), this value is still nowhere near the ~+1‰ fractionation factor needed to explain the isotope effects in the individual zircons and baddeleyite of the FC-1 gabbro (Fig. 6, Ibañez-Mejia and Tissot, 2019).

An upper limit can be independently placed on the magnitude of NFS effects potentially affecting the published zircon and baddeleyite data from Ibañez-Mejia and Tissot (2019) and Tompkins et al. (2020). In both studies, a double-spike (DS) method was used to quantify the mass-dependent Zr isotope fractionation of the samples ($\delta^{94/90}$Zr). The presence of mass-independent anomalies, if unaccounted for during DS data reduction, would result in inaccurate estimates for the extent of mass-dependent fractionation (Eugster et al., 1969; Niederer et al., 1985; Burkhardt et al., 2014; Greber et al., 2017; Hu and Dauphas, 2017). Typically for double-spike data reduction, only 4 isotopes (3 isotope ratios) are considered, providing an exact solution to the three unknowns being solved for (*i.e.*, the proportion of spike, instrumental mass-bias and natural mass bias between the sample and the standard). For such scenarii, Hu and Dauphas (2017) derived analytical equations that rigorously estimate the corrections on delta values required by the presence of isotopic anomalies. In the Ibañez-Mejia and Tissot (2019) and Tompkins et al. (2020) work, however, all 5 isotopes of Zr are used in a minimization scheme to perform the DS data reduction, implying that an exact solution not always necessarily exists and that the impact of mass-independent effects on delta values must be assessed numerically. As detailed in Tompkins et al. (2020), a 4-ratio minimization scheme provides a way to check for the presence of mass-independent effects (relative to the normalizing standard), which would manifest as isotopic anomalies even after data reduction. For all samples measured in these two studies, all isotope ratios were found to be mass-dependent within uncertainty (~±0.01‰/amu), thus allowing calculation of a maximum permissible NFS effect to these data, as detailed below.

Assuming that the pattern of NFS isotopic effects scales as the ^{90}Zr-^{94}Zr normalized $\delta\langle r^2\rangle$ shown in Fig. 7b, isotopic anomalies of increasing magnitude were (numerically) added to the isotopic composition of the Zr standard to simulate the presence of NFS effects, and these anomalous standards were mixed in ideal proportion with the DS. For each mixture in this hypothetical dataset, the DS data reduction was performed using the minimization approach described in Tompkins et al. (2020), and the difference between the algorithm solution and standard composition was calculated. The results of these calculations are plotted in Figs. 8 and 9. The observed mass-dependency of all Zr isotope ratios within ±0.01‰/amu in the Ibañez-Mejia and Tissot (2019) and Tompkins et al. (2020) datasets, places tight constraints on the apparent mass-dependent fractionation that can be attributed to NFS effects. Considering the calculations shown in Fig. 8, at most 0.001–0.002‰/amu effects are permissible, above which the ^{92}Zr/^{90}Zr ratio would no longer be mass-dependently related to the other Zr isotope ratios. This indicates that (i) NFS effects were not a significant driver of isotopic fractionation in these samples, which display much larger mass-dependent effects (from 0.014 to 0.250‰/amu), and (ii) that NFS-induced mass-independent effects in the samples, expressed in epsilon notation as ε^{91}Zr, ε^{92}Zr and ε^{96}Zr anomalies ($\varepsilon^{9x}\mathrm{Zr} = [(^{9x}\mathrm{Zr}/^{90}\mathrm{Zr}_{\mathrm{Standard+NFS}}/^{9x}\mathrm{Zr}/^{90}\mathrm{Zr}_{\mathrm{Standard}}) - 1] * 10^4$), were smaller than, respectively, ~−4.6, +0.4 and −5.2 ε-units (Figs. 8 and 9).

5.3. Kinetic effects as drivers of Zr isotope fractionation

In addition to the thermodynamic (equilibrium) effects described above, stable isotope fractionation amongst phases in high-T environments can also be driven by the mass-dependency of reaction rate constants or self-diffusion coefficients in solids and liquids (*i.e.*, kinetic isotope effects; see reviews by Richter et al., 2009a; Watkins et al., 2017). Mineral growth from a crystallizing magma is a first-order process known to result in compositional (*e.g.*, Albarede and Bottinga, 1972) and isotopic (*e.g.*, Watson and Müller, 2009) disequilibrium effects for major

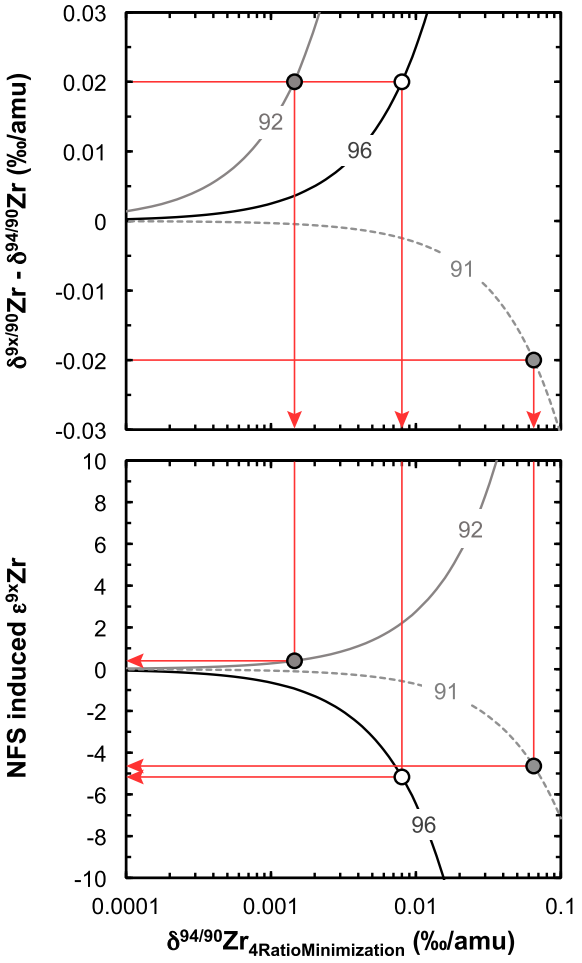

Fig. 8. (Top) Offset in mass-dependent Zr isotope composition after DS data reduction (expressed as $\delta^{9x/90}$Zr-$\delta^{94/90}$Zr, in ‰/amu, with $x = 1$, 2, or 6) and (bottom) NFS induced mass-independent effects (in epsilon notation, $\varepsilon^{9x}Zr = (^{9x/90}Zr)_{standard+NFS}/(^{9x/90}Zr)_{standard} - 1) * 10^4$) as a function of the $\delta^{94/90}$Zr obtained using a 4 ratio minimization DS reduction. The mass-dependency of all ratios, within ± 0.01‰/amu in zircons measured to date (Ibañez-Mejia and Tissot, 2019; Tompkins et al., 2020) indicates that NFS effects were not the dominant driver of isotopic fractionation in these samples. The maximum permissible offset of 0.02‰/amu between $\delta^{9x/90}$Zr and $\delta^{94/90}$Zr values, provides (red arrows) upper limits of −4.6 ε^{91}Zr, +0.4 ε^{92}Zr and −5.2 ε^{96}Zr on the NFS induced anomalies in these samples.

and trace elements. These fractionations arise from a kinetic imbalance between crystal growth, chemical diffusion in the melt, and the isotopic mass dependency of diffusion. As shown by Albarede and Bottinga (1972), for elements with equilibrium fractionation coefficients (K_{eq}) between solid and melt smaller than unity, a 'pile-up' of the species of interest occurs near the moving solid–liquid interface when diffusion is too slow to maintain a uniform concentration throughout the liquid. Conversely, for elements with $K_{eq} > 1$ in the crystallizing solid, growth of the mineral will deplete that species in the surrounding melt, inducing a 'draw down' near the moving solid–liquid interface. The concentration gradients that develop as the

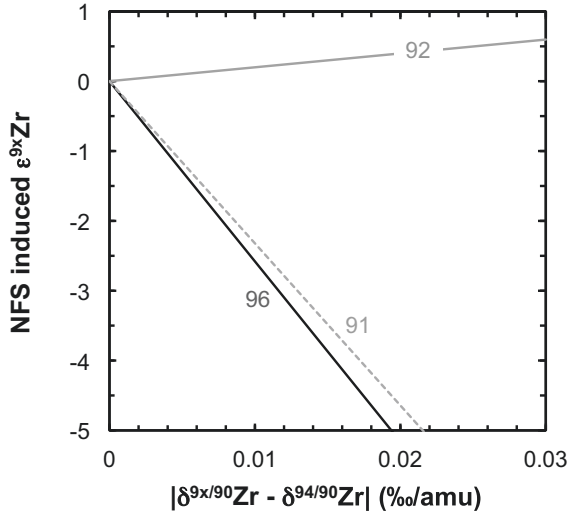

Fig. 9. NFS induced mass-independent effects (expressed using the epsilon notation) as a function of the offset in mass-dependent Zr isotope composition after DS data reduction (expressed as the absolute value of $\delta^{9x/90}$Zr-$\delta^{94/90}$Zr, in ‰/amu, with $x = 1$, 2, or 6).

solid grows lead to diffusive fluxes within the liquid (Tiller et al., 1953; Smith et al., 1955; Albarede and Bottinga, 1972), and such regions are known as diffusive boundary layers (DBLs) (Watson and Müller, 2009; Watkins et al., 2017).

Zirconium is a moderately to highly incompatible lithophile element with K_{eq} values smaller than unity for most rock-forming phases growing from a silicate melt (see data compilation of Keller et al., 2017). Thus, as a magma cools and fractionally crystallizes, this incompatibility results in a progressive Zr enrichment in differentiated liquids. For instance, in the case of the Duluth Complex FC-1 anorthositic gabbro, magma crystallization is dominated by the initial growth of plagioclase, followed by intra-cumulus growth of clinopyroxene and Fe-Ti oxides within trapped melt pockets (Ibañez-Mejia and Tissot, 2019). Zr is extremely incompatible in plagioclase ($K_{eq} < 0.01$; *e.g.*, Bindeman and Davis, 2000; Nielsen et al., 2017), strongly to moderately incompatible in clinopyroxene ($K_{eq} = 0.12$–0.27; *e.g.*, Watson and Ryerson, 1986; Hart and Dunn, 1993; Huang et al., 2006), and moderately incompatible in ilmenite ($K_{eq} = 0.33$–0.80; *e.g.*, Nakamura et al., 1986; Klemme et al., 2006). Therefore, growth of all these phases from a magma will lead to an overall Zr enrichment in the residual liquid, as well as the development of markedly enriched DBLs around the crystallizing phases. To illustrate this, Fig. 10 shows an example calculation of the [Zr] profiles that would develop in a solid (left) and coexisting liquid (right) during clinopyroxene crystal growth at isothermal conditions, as a function of variable boundary migration velocities (v) expressed in cm/Myr. These calculations clearly illustrate that the magnitude of the concentration gradient that develops, and therefore the resulting diffusive flux, are proportional to v (or the v/D ratio). Furthermore, DBLs such as those shown in Fig. 10 will be the most likely regions of zircon nucleation during

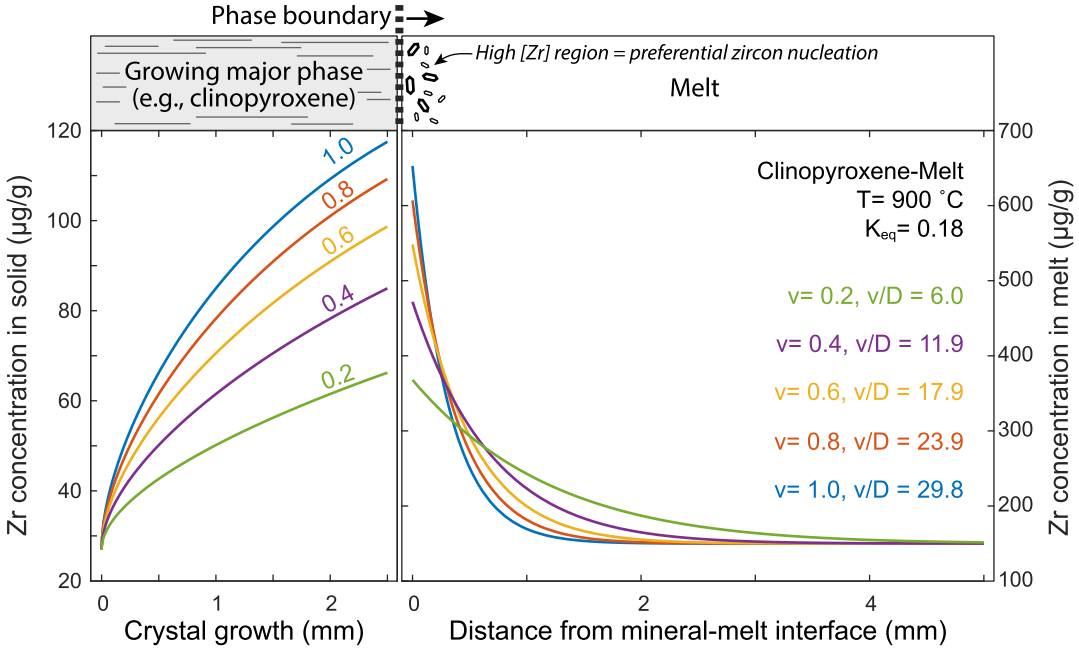

Fig. 10. [Zr] profiles during crystal growth in a melt, calculated using a clinopyroxene-melt partition coefficient (K_{eq}) of 0.18 and crystal growth velocities ranging from 0.2 to 1.0 cm/Myr. (Left) Concentration profiles developed within the growing solid. (Right) Concentration profiles developed within the liquid, as driven by concurrent solid growth and diffusion. Calculations used the clinopyroxene/melt K_{eq} of Huang et al. (2006), the Zr diffusion parameters in dry melts of Mungall et al. (1999), and the analytical solution to the linear 1-D diffusion equation with a moving boundary of Smith et al. (1955). Note the break in vertical and horizontal scales between the two plots. (Top) Illustration of how growth of a major rock-forming phase with a low (<1) K_{eq} for Zr (e.g., clinopyroxene) leads to preferential zircon nucleation within high [Zr] diffusive boundary layers in the melt.

magmatic crystallization, owing to their much higher [Zr] and the concentration dependence of zircon saturation in silicate liquids (Boehnke et al., 2013).

Kinetic theory predicts that the ratio of the diffusivities of two isotopes in an ideal gas is proportional to the square root of the ratio of their masses (*i.e.*, $D_1/D_2 = \sqrt{[m1/m2]}$), but for condensed systems this formulation overstates the mass-dependency of diffusion due to non-negligible interactions between the diffusing species and their nearest neighbors (Richter et al., 1999). Thus, for aqueous solutions and silicate melts it has been customary to express the ratio of the self-diffusivities using an inverse power-law function:

$$\frac{D_2}{D_1} = \left(\frac{m_1}{m_2}\right)^{\beta} \quad (3)$$

where D_x are the diffusivities of the two isotopes in question, m_x are their respective masses, and β is a dimensionless empirical parameter that expresses the efficiency of diffusive isotope fractionation (Richter et al., 1999). This last term should not be confused with the β-factors presented in Figs. 3 and 5, which characterize the equilibrium isotopic fractionation between two phases. Although no experimental data yet exist for constraining β (in Eq. (3)) in silicate melts for elements heavier than Fe (Richter et al., 2003, 2008, 2009b; Watkins et al., 2014), or for trace elements other than Li (Richter et al., 2003, 2014), some useful approximations can be made from the existing data: (i) the overall range of β factors for various elements in silicate melts is between 0 and 0.22 (see recent review in Watkins et al., 2017); and (ii) the efficiency of diffusive fractionation scales proportionally to the diffusivity of the species of interest normalized to the diffusivity of the solvent, or Si in the case of silicate liquids (Watkins et al., 2011). Baker (1990) performed chemical interdiffusion experiments between dacitic and rhyolitic melts at 1 and 10 kbar, and simultaneously determined the diffusivities of Zr and Si at varying SiO_2 concentrations. He found the Zr diffusivity to be invariably faster than that of Si, with average D_{Zr}/D_{Si} of 1.43, 1.62 and 2.01 for SiO_2 contents of 65, 70 and 75 wt. %, respectively. When compared with the solvent-normalized diffusivities and β coefficients experimentally determined for Ca, Mg and Fe, these experimental D_{Zr}/D_{Si} ratios fall within a range where the β coefficients for major elements vary between 0.03 and 0.1 (Fig. 11). As low abundance elements exhibit, in general, higher mass discrimination (*i.e.*, higher β coefficients) than major elements (Richter et al., 2003, 2008, 2009b; Watkins et al., 2009, 2011), the experimental D_{Zr}/D_{Si} values shown in Fig. 11 suggest that the β values for Zr in silicate melts may in fact be non-negligible.

5.3.1. The FC-1 (Duluth Gabbro) case: can diffusion explain its extreme $\delta^{94/90}$Zr variability?

Given the faster diffusion of lighter isotopes, the intuitive expectation for a phase growing from a melt under simple diffusion-controlled conditions (*e.g.*, Bindeman and Melnik, 2016) is that its bulk composition should be lighter than that of the initial liquid from which it precipitated. In

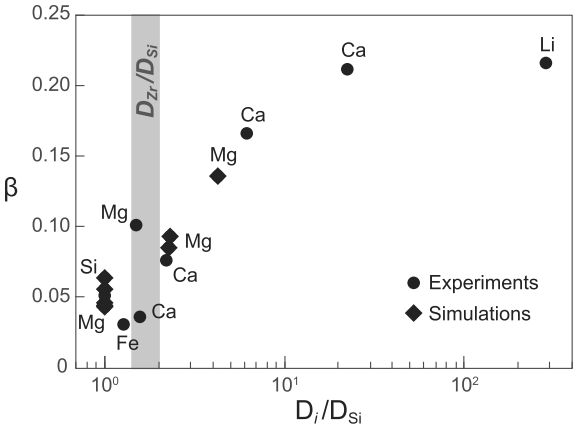

Fig. 11. Efficiency of diffusive isotope fractionation (β) in silicate melts vs. solvent-normalized diffusivity (modified from Watkins et al., 2017 and references therein). Gray shaded region shows the range of experimental D_{Zr}/D_{Si} in dacitic to rhyolitic melts (i.e., SiO_2 wt.% from 65 to 75) at 10 kbar pressure (after Baker, 1990), suggesting that β_{Zr} might be non-negligible (between 0.01 and 0.10).

stark contrast, the zircon and baddeleyite crystals from the Duluth complex (Ibañez-Mejia and Tissot, 2019) display extreme $\delta^{94/90}$Zr variability, and are mainly heavier, compared to their host rock (assumed to represent the starting magma composition).

To explore the potential role of diffusive fractionation as a driver of large mass-dependent Zr isotope variations, such as those observed in the FC-1 gabbro (Ibañez-Mejia and Tissot, 2019), we performed a series of exploratory calculations using parameters relevant to FC-1 crystallization. The diffusivity of Zr at 900 °C, which is the zircon crystallization maxima for this sample as determined from Ti-in-zircon thermometry (Hiess et al., 2008) and thermodynamic modelling (Ibañez-Mejia and Tissot, 2019), was calculated using the 'dry' experimental parameters of Mungall et al. (1999). To constrain a reasonable range of moving boundary velocities, we observe that the maximum timescale of zircon crystallization determined from high-precision U-Pb dating of FC-1 is ca. 220 kyr and that intra-cumulus phase assemblages (*i.e.*, clinopyroxene, ilmenite) in this rock reach up to ca. 0.25 cm in diameter (Ibañez-Mejia and Tissot, 2019). Thus, a maximum boundary migration velocity during the interval recorded by zircon crystallization should be on the order of ~1 cm/Myr for the largest melt pockets, or possibly slower for smaller pockets. To account for this variability, calculations were performed for v values from 1.0 down to 0.2 cm/Myr. Similarly, and based on the observations summarized in Fig. 11, β_{Zr} values ranging from 0.01 to 0.05 were used to account for the uncertainty of this entirely unconstrained parameter. Two cases were considered: a moving plagioclase-melt boundary ($K_{eq} = 0.004$; Bindeman and Davis, 2000) and a clinopyroxene-melt boundary ($K_{eq} = 0.18$; Huang et al., 2006).

The results of these calculations are summarized in Fig. 12, which show the isotopic profiles that would develop in a melt as a function of the identity of the growing solid, and the variable values of v and β_{Zr}. Intuitively, one might expect that, as the DBL becomes enriched in Zr (*e.g.*, Fig. 10), faster diffusion of lighter isotopes away from the boundary would render the DBL isotopically heavy towards the mineral-melt interface, and isotopically light away from the interface (*i.e.*, towards the tail of the DBL). The results shown in Fig. 12 confirm that this is indeed the case, and that reasonable combinations of v, β_{Zr}, and K_{eq} have the potential to produce per-mil level $\delta^{94/90}$Zr variations. For similar v/D values, plagioclase-melt boundaries (*i.e.*, lower K_{eq} interfaces) would, in general, result in larger magnitudes of stable isotope fractionation within the DBL relative to phases with higher K_{eq}, such as clinopyroxene. Likewise, faster boundary migration velocities (higher v/D) would result in larger magnitudes of isotope fractionation, as would also be the case for larger magnitudes of β_{Zr} (*i.e.*, lower D^H/D^L). Because zircon saturation in the melt is directly dependent on [Zr] (Boehnke et al., 2013), this mineral would be more likely to nucleate within the DBLs rather than away from them, as 'background' [Zr] in the liquid would remain systematically lower. This observation implies that, throughout the fractional crystallization history of FC-1, zircon would be more likely to grow in regions of the melt that are enriched in heavy Zr isotopes rather than in isotopically 'normal' regions, as the latter would be accompanied by significantly lower [Zr]. Therefore, even if the equilibrium fractionation factor $\Delta^{94/90}Zr_{zircon\text{-}melt}$ is essentially negligible (Sections 4.1 and 4.2), kinetic isotopic fractionation effects within the DBLs that develop during fractional crystallization can explain the preferential formation of isotopically heavy zircon, and thus the distribution of $\delta^{94/90}$Zr values in FC-1 zircon and baddeleyite (Ibañez-Mejia and Tissot, 2019).

5.3.2. The case of negligible (Mud Tank) and negative (Gangdese) fractionation values

Kinetic controls could also explain the $\delta^{94/90}$Zr results obtained in zircon from the Mud Tank carbonatite (Tompkins et al., 2020) and the Gangdese arc, Tibet (Guo et al., 2020), which suggest negligible to negative $\Delta^{94/90}Zr_{zircon\text{-}melt}$ values, respectively (Fig. 6). Unlike FC-1 zircon, which likely grew within isotopically heavy diffusive boundary layers developed during extensive magmatic fractional crystallization (Section 5.3.1), zircon crystals from the Gangdese arc, Tibet (Guo et al., 2020), exhibit apparent light-to-heavy $\delta^{94/90}$Zr profiles from core to rim. Such profiles would be generally consistent with simple diffusion of Zr from the melt towards the crystallizing solid (*e.g.*, Bindeman and Melnik, 2016), which would result in lighter isotopes to be concentrated near the core of a growing crystal and progressively heavy compositions towards the rim (*e.g.*, Watson and Müller, 2009). Guo et al. (2020) discarded the possibility that their measured profiles could result from a kinetic control to Zr isotope fractionation arguing that: (i) Zr diffusivities in magmas (D) and typical radial zircon growth rates (R) usually yield R/D < 0.01 cm^{-1}, which would be expected to produce only minor diffusive isotope fractionation effects (Watson and Müller, 2009), and (ii) the absence of 'W' shaped profiles from their zircon transects indicates the lack of a kinetic control. There are multiple issues with these interpretations,

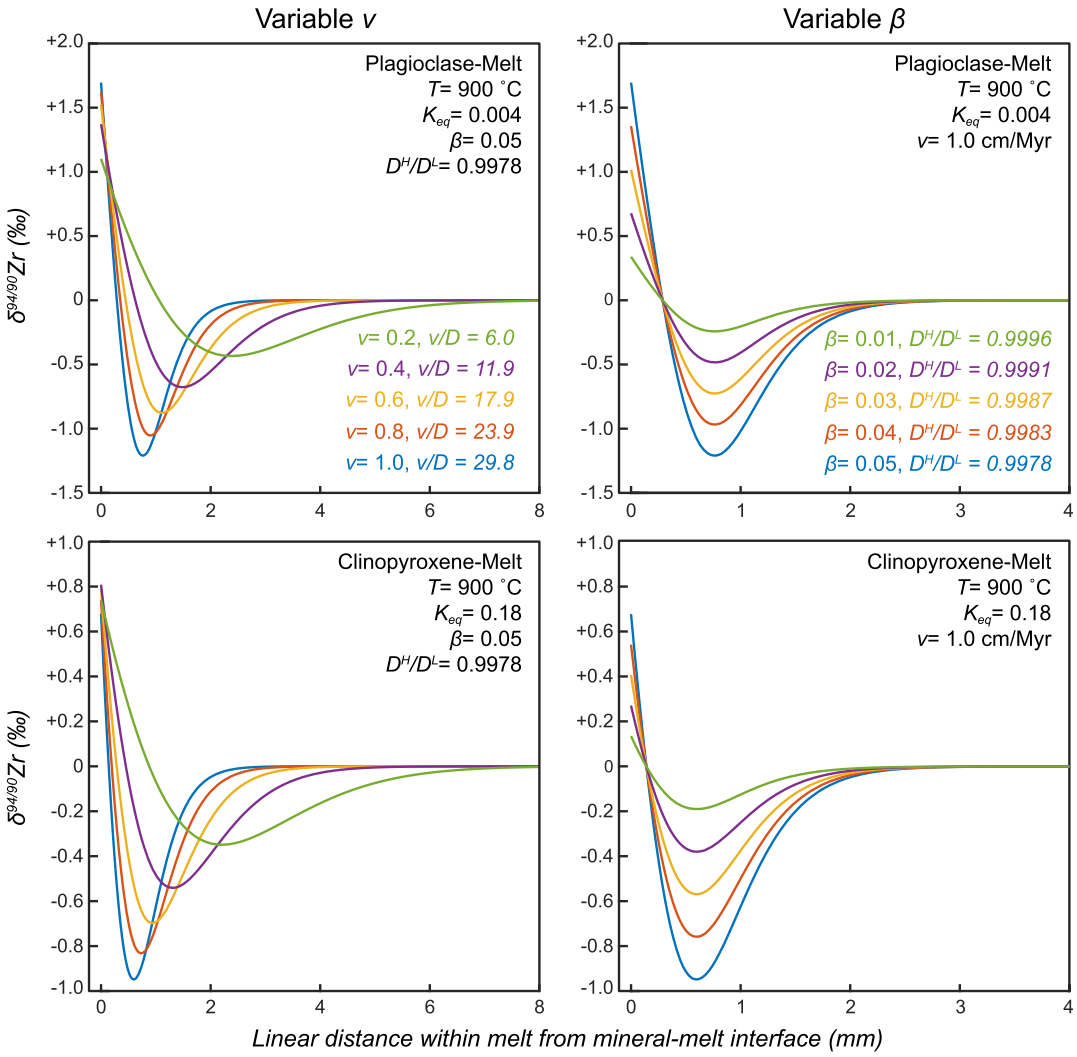

Fig. 12. $^{94/90}$Zr profiles developed in a silicate melt due to kinetic (diffusive) isotopic fractionation in the liquid driven by crystallization of plagioclase (top) and clinopyroxene (bottom). (Left) Effects of variable solid growth velocity (v) at a constant $\beta_{Zr} = 0.05$. (Right) Effects of variable β_{Zr} at a constant solid growth velocity ($v = 1$ cm/Myr). Preferential zircon saturation in high [Zr] regions of the diffusive boundary layers (i.e., nearest to the mineral-melt interface; see Fig. 10) will lead to the formation of isotopically heavy zircon.

but most importantly: (i) radial growth rates for zircon, which have been suggested to be on the order of 10^{-13}-10^{-17} cm/s (Watson, 1996; Schmitt et al., 2011), when divided by Zr diffusivities in a liquid at relevant magmatic temperatures for the Gangdese samples (*e.g.*, $\sim 3.5 \times 10^{-18}$ cm^2/s at 740 °C, calculated using the diffusion parameters of Mungall et al., 1999), result in R/D values on the order of 2.9×10^5 to 2.8×10^1 cm^{-1}, which are well within the range where large diffusive isotope fractionations can be expected based on the calculations of Watson and Müller (2009); (ii) the initial drop in isotopic composition away from the geochemical core of a growing zircon crystal – which would produce the W-shaped pattern – would be extremely steep as a function of radial position for the large R/D and K_{eq} values involved during zircon growth. This means that a clear 'W' shape profile would be difficult – if not impossible – to resolve at the spatial resolution of the Guo et al. (2020) LA-ICP-MS analyses, potentially leading to convoluted signals and poorly-resolved W shapes such as those observed in several of their profiles. Given these considerations, the observations made by Guo et al. (2020) cannot in fact rule out a kinetic control on the measured $\delta^{94/90}$Zr and calculated $\alpha_{zircon\text{-}melt}$ values. This, in addition to the much smaller $\Delta^{94/90}Zr_{zircon\text{-}melt}$ found from our *ab initio* calculations, clearly point to the Guo et al. (2020) profiles as being kinetically controlled rather than produced *via* equilibrium isotope fractionation.

Unlike the FC-1 and Gangdese arc zircon, which formed from silicate melts, the Mud Tank zircon studied by Tompkins et al. (2020) is a ~732 Ma megacryst crystallized from a carbonatite melt (Crohn and Moore, 1984). This zircon displays remarkably homogeneous $\delta^{94/90}$Zr values, suggesting a lack of equilibrium and/or kinetic isotopic fractionation between zircon and melt. The lack of

equilibrium fractionation is well explained by our *ab initio* calculations (Section 4.2), but the lack of kinetic effects deserves further discussion. Differences in kinetic fractionation effects might stem from the peculiar composition of carbonatite magmas, the diffusive properties of Zr, and/or the timescales of megacrystic zircon growth. For instance, if the diffusivity of Zr in carbonatite melts is much larger than in silicate melts, such that any diffusive boundary layers in a crystallizing carbonatite are rapidly homogenized relative to the zircon growth velocity (*i.e.*, negligible v/D), this would lead to insignificant kinetic fractionation effects to be recorded in the solid (Watkins et al., 2017). Alternatively, the contrasting abundance of SiO_2 between carbonatite and silicate melts could influence zircon formation. In silicate melts, Si is in the majority of cases the most abundant cation, and so zircon growth should be limited by the supply of Zr to a growing seed, rather than by Si availability and diffusivity. On the other hand, in carbonatite melts, SiO_2 can be as low as 2–5 wt.%, and thus its availability may also play a role in the kinetics of zircon crystallization. If Zr diffuses faster than Si in carbonatite magmas as it does in silicate melts (Fig. 11), then zircon growth in carbonatites could be controlled by Si diffusion rather than Zr diffusion, thus allowing more time for Zr to maintain isotopic equilibrium throughout the melt and with the crystallizing phases. To our knowledge, however, Zr and Si diffusion coefficients have so far not been constrained in carbonatite melts, so the plausibility of this hypothesis cannot yet be verified. These remarks underline the determining importance of the status of an element (trace vs. major) on its fractionation properties. This importance was emphasized and discussed in a very different situation, for the fractionation of trace (Ba, Sr, B, Li) and major (Mg, Ca) elements during the precipitation of carbonates (calcite, aragonite) at low temperatures (Mavromatis et al., 2013).

In summary, although no experimental data yet exist for determining β_{Zr} in silicate liquids, the exploratory calculations made here suggest that reasonable combinations of v, β_{Zr}, and K_{eq} have the potential to produce per-mil $\delta^{94/90}$Zr values in crystallizing magmas. As such, kinetic effects are at present the most likely explanation for the large (and variable) mass-dependent Zr isotope variations observed amongst zircon and baddeleyite from silicate melts (see Fig. 6), and might also explain the lack of isotopic zoning in megacrystic zircon from the Mud Tank carbonatite.

5.4. Future directions and concluding remarks

The limited magnitude of Zr isotope fractionation predicted by our *ab initio* calculations and inferences on NFS effects are consistent with the homogeneous $\delta^{94/90}$Zr values of some zircon localities, such as Mud Tank, 91,500 and Plesovice. However, these fail to explain the large isotope variations observed in several other igneous systems such as the Duluth Complex, Hekla volcano, and the Gangdese arc batholith (Fig. 6). On the other hand, Zr diffusion in response to concentration gradients developed within silicate liquids by rock-forming phase crystallization, and/or zircon nucleation and growth, seems to provide a more plausible mechanism to explain large isotopic effects in igneous minerals.

Building from the observations made here, future studies should target the assumptions and testable predictions of the diffusive fractionation hypothesis. In particular:

1) Experimental determination of β_{Zr} values in silicate liquids, as well as β_{Zr} values and the relative diffusivities of Zr and Si in carbonatite liquids, will be needed to evaluate the hypotheses outlined here regarding the Duluth gabbro and Mud Tank systems.
2) Major phases with low Zr partition coefficient (*e.g.*, plagioclase, clinopyroxene) should display diagnostic concentration and isotopic profiles, with both [Zr] and $\delta^{94/90}$Zr values increasing in the direction of solid-melt boundary propagation. Coupled with adequate modeling, spatially-resolved (*e.g.*, LA-ICPMS) investigations could provide a robust test of the diffusion hypotheses put forth here.
3) Zircon and baddeleyite formed near the interface between major phases and melt should display elevated $\delta^{94/90}$Zr values, while crystals formed further away from the boundary may record either unfractionated or lower $\delta^{94/90}$Zr values. In-situ isotope measurements of Zr-bearing phases using LA-ICPMS or SIMS techniques can be used to test such spatial distributions of $\delta^{94/90}$Zr values in a petrologic context.

Another aspect needing further work is the possibility that some rock forming minerals which can incorporate a significant amount of Zr (*e.g.*, clinopyroxene, ilmenite), could fractionate Zr isotopes. *Ab initio* calculations could not be performed for these minerals, owing to two main limitations. (i) First is the general lack of knowledge on the host site of Zr in these mineral structures. Taking the example of pyroxene, Zr^{4+} could substitute either in the M1 or M2 site (Morimoto, 1988) for elements like Mg^{2+}, Ca^{2+}, Na^{+} or Li^{+}. This would require, at least Zr^{4+}-Mg^{2+} substitution coupled to, for instance, two Al^{3+}-Si^{4+} substitutions (or one Al^{3+}-Si^{4+} plus one Na^{+}-Ca^{2+}) to preserve charge balance. The large number of possible substitutions, challenges associated with proper computation of the isotope properties of such non-isoelectronic cation substitution, as well as the extremely large unit-cell to consider to obtain realistic results (to account for the dilution of Zr) make such calculations prohibitively difficult. (ii) Assuming sufficient computational power, the lack of constraints on the vibrational (and other) properties of Zr in these minerals would make it virtually impossible to validate the model results. Based on the large variety of Zr environments tested here, and on the very low fractionations obtained in all instances, we do not expect these additional calculations to yield fractionation coefficients that are sufficiently large to explain the natural observations by equilibrium mechanisms alone. Yet, to test these assumptions and evaluate whether Zr isotope fractionation is associated with Zr uptake into major rock forming minerals, future studies could perform high-precision Zr isotope analyses on clean

mineral separates. Such investigations in rock samples from well-characterized igneous systems could help establish whether such fractionation factors are dependent on the composition, temperature, water content, crystallization timescales and/or redox conditions of the melt.

The nascent field of mass-dependent Zr stable isotope variations is rapidly expanding. As a growing number of studies document the natural variations of $\delta^{94/90}$Zr in igneous, metamorphic and sedimentary systems, elucidating the mechanisms responsible for the partitioning of Zr isotopes will become increasingly critical. Our work suggests that kinetic processes, particularly diffusive fractionation, are likely to play a dominant role in driving variability in Zr-bearing phases in high-T environments. This is a critical first step which, together with future studies, will help establish a robust framework to interpret the petrogenetic significance of fractionated Zr isotopic compositions.

Declaration of Competing Interest

The authors declare that they have no known competing financial interests or personal relationships that could have appeared to influence the work reported in this paper.

ACKNOWLEDGEMENT

This research was supported by NSF-EAR grants 1823748 (to MIM) and 1824002 (to FT) and start-up funds to MIM provided by University of Rochester and to FT provided by Caltech. This work was performed using HPC resources from CALMIP (Calcul en Midi-Pyrénées; Grant 2019-P1037). We are grateful for critical evaluations from Editor Mark Rehkämper, Jörn-Frederik Wotzlaw, and two anonymous reviewers, which helped to improve the clarity of this manuscript.

APPENDIX A. SUPPLEMENTARY MATERIAL

Supplementary data to this article can be found online at https://doi.org/10.1016/j.gca.2020.09.028.

REFERENCES

Abe Minor, Suzuki Tatsuy, Fujii Yasuhik, Hada Masahik and Hirao Kimihik (2008) An ab initio molecular orbital study of the nuclear volume effects in uranium isotope fractionations. *J. Chem. Phys.* **129**, 164309. https://doi.org/10.1063/1.2992616.

Abrahams S. C. and Bernstein J. L. (1971) Rutile: normal probability plot analysis and accurate measurement of crystal structure. *J. Chem. Phys.* **55**(7), 3206–3211. https://doi.org/10.1063/1.1676569.

Akram W. and Schönbächler M. (2016) Zirconium isotope constraints on the composition of Theia and current Moon-forming theories. *Earth Planet. Sci. Lett.* **449**, 302–310. https://doi.org/10.1016/j.epsl.2016.05.022.

Albarede F. and Bottinga Y. (1972) Kinetic disequilibrium in trace element partitioning between phenocrysts and host lava. *Geochim. Cosmochim. Acta* **36**, 141–156. https://doi.org/10.1016/0016-7037(72)90003-8.

Angeli I., Gangrsky Y. P., Marinova K. P., Boboshin I. N., Komarov S. Y., Ishkhanov B. S. and Varlamov V. V. (2009) N and Z dependence of nuclear charge radii. *J. Phys. G Nucl. Part. Phys.* **36**. https://doi.org/10.1088/0954-3899/36/8/085102 085102.

Angeli I. and Marinova K. P. (2013) Table of experimental nuclear ground state charge radii: an update. *At. Data Nucl. Data Tables* **99**, 69–95. https://doi.org/10.1016/j.adt.2011.12.006.

Baker D. R. (1990) Chemical interdiffusion of dacite and rhyolite: anhydrous measurements at 1 atm and 10 kbar, application of transition state theory, and diffusion in zoned magma chambers. *Contrib. Mineral. Petrol.* **104**, 407–423. https://doi.org/10.1007/BF01575619.

Balan E., Saitta A. M., Mauri F. and Calas G. (2001) First-principles modeling of the infrared spectrum of kaolinite. *Am. Mineral.* **86**, 1321–1330. https://doi.org/10.2138/am-2001-11-1201.

Baroni S., de Gironcoli S., Dal Corso A. and Giannozzi P. (2001) Phonons and related crystal properties from density-functional perturbation theory. *Rev. Mod. Phys.* **73**, 515–562. https://doi.org/10.1103/RevModPhys.73.515.

Bergquist B. A. and Blum J. D. (2007) Mass-dependent and -independent fractionation of hg isotopes by photoreduction in aquatic systems. *Science* **318**, 417–420. https://doi.org/10.1126/science.1148050.

Bigeleisen J. (1996) Nuclear size and shape effects in chemical reactions. Isotope chemistry of the heavy elements. *J. Am. Chem. Soc.* **118**, 3676–3680. https://doi.org/10.1021/ja954076k.

Bigeleisen J. and Mayer M. G. (1947) Calculation of equilibrium constants for isotopic exchange reactions. *J. Chem. Phys.* **15**, 261–267. https://doi.org/10.1063/1.1746492.

Bindeman I. N. and Davis A. M. (2000) Trace element partitioning between plagioclase and melt: investigation of dopant influence on partition behavior. *Geochim. Cosmochim. Acta* **64**, 2863–2878. https://doi.org/10.1016/S0016-7037(00)00389-6.

Bindeman I. N. and Melnik O. E. (2016) Zircon Survival, rebirth and recycling during crustal melting, magma crystallization, and mixing based on numerical modelling. *J. Petrol.* **57**, 437–460. https://doi.org/10.1093/petrology/egw013.

Blanchard M., Balan E. and Schauble E. A. (2017) Equilibrium fractionation of non-traditional isotopes: a molecular modeling perspective. *Rev. Mineral. Geochem.* **82**, 27–63. https://doi.org/10.2138/rmg.2017.82.2.

Boehnke P., Watson E. B., Trail D., Harrison T. M. and Schmitt A. K. (2013) Zircon saturation re-revisited. *Chem. Geol.* **351**, 324–334. https://doi.org/10.1016/j.chemgeo.2013.05.028.

Burkhardt C., Hin R. C., Kleine T. and Bourdon B. (2014) Evidence for Mo isotope fractionation in the solar nebula and during planetary differentiation. *Earth Planet. Sci. Lett.* **391**, 201–211. https://doi.org/10.1016/j.epsl.2014.01.037.

Carlone C. (1992) Raman spectrum of zirconia-hafnia mixed crystals. *Phys. Rev. B* **45**, 2079–2084. https://doi.org/10.1103/PhysRevB.45.2079.

Crohn P. W. and Moore D. H. (1984) The mud tank carbonatite, strangways range, central Australia. *BMR J. Aust. Geol. Geophys.* **9**, 13–18.

Dal Corso A. (2014) Pseudopotentials periodic table: from H to Pu. *Comput. Mater. Sci.* **95**, 337–350. https://doi.org/10.1016/j.commatsci.2014.07.043.

Dauphas N., Roskosz M., Alp E. E., Golden D. C., Sio C. K., Tissot F. L. H., Hu M. Y., Zhao J., Gao L. and Morris R. V. (2012) A general moment NRIXS approach to the determination of equilibrium Fe isotopic fractionation factors: application to goethite and jarosite. *Geochim. Cosmochim. Acta* **94**, 254–275.

Dauphas N., Hu M. Y., Baker E. M., Hu J., Tissot F. L., Alp E. E., Roskosz M., Zhao J., Bi W., Liu J. and Lin J. F. (2018) SciPhon: a data analysis software for nuclear resonant inelastic X-ray scattering with applications to Fe, Kr, Sn, Eu and Dy. *J. Synchrotron Radiat.* **25**(5), 1581–1599.

Dupuis R., Benoit M., Nardin E. and Méheut M. (2015) Fractionation of silicon isotopes in liquids: the importance of configurational disorder. *Chem. Geol.* **396**, 239–254. https://doi.org/10.1016/j.chemgeo.2014.12.027.

Eugster O., Tera F. and Wasserburg G. J. (1969) Isotopic analyses of barium in meteorites and in terrestrial samples. *J. Geophys. Res. 1896–1977*(74), 3897–3908. https://doi.org/10.1029/JB074i015p03897.

Fadda G., Colombo L. and Zanzotto G. (2009) First-principles study of the structural and elastic properties of zirconia. *Phys. Rev. B* **79**. https://doi.org/10.1103/PhysRevB.79.214102 214102.

Fadda G., Zanzotto G. and Colombo L. (2010a) First-principles study of the effect of pressure on the five zirconia polymorphs. I. Structural, vibrational, and thermoelastic properties. *Phys. Rev. B* **82**. https://doi.org/10.1103/PhysRevB.82.064105 064105.

Fadda G., Zanzotto G. and Colombo L. (2010b) First-principles study of the effect of pressure on the five zirconia polymorphs. II. Static dielectric properties and Raman spectra. *Phys. Rev. B* **82**. https://doi.org/10.1103/PhysRevB.82.064106 064106.

Farges F., Ponader C. W. and Brown G. E. (1991) Structural environments of incompatible elements in silicate glass/melt systems: I. Zirconium at trace levels. *Geochim. Cosmochim. Acta* **55**, 1563–1574. https://doi.org/10.1016/0016-7037(91)90128-R.

Farges F. (1996) Does Zr–F "complexation" occur in magmas? *Chem. Geol.* **127**(4), 253–268. https://doi.org/10.1016/0009-2541(95)00132-8.

Farges F., Brown, Jr., G. E. and Rehr J. J. (1996) Coordination chemistry of Ti(IV) in silicate glasses and melts: I. XAFS study of titanium coordination in oxide model compounds. *Geochim. Cosmochim. Acta* **60**(16), 3023–3038. https://doi.org/10.1016/0016-7037(96)00144-5.

Feng L., Hu W., Jiao Y., Zhou L., Zhang W., Hu Z. and Liu Y. (2020) High-precision stable zirconium isotope ratio measurements by double spike thermal ionization mass spectrometry. *J. Anal. Atomic Spectrom.* **88**, 293–310. https://doi.org/10.1039/C9JA00385A.

Fujii T., Moynier F. and Albarède F. (2006a) Nuclear field vs. nucleosynthetic effects as cause of isotopic anomalies in the early Solar System. *Earth Planet. Sci. Lett.* **247**, 1–9. https://doi.org/10.1016/j.epsl.2006.04.034.

Fujii T., Moynier F., Telouk P. and Albarède F. (2009) Nuclear field shift effect in the isotope exchange reaction of cadmium using a crown ether. *Chem. Geol. Adv. Exp. Theor. Isotope Geochem.* **267**, 157–163. https://doi.org/10.1016/j.chemgeo.2008.12.004.

Fujii T., Moynier F., Telouk P. and Albarède F. (2006b) Mass-independent isotope fractionation of molybdenum and ruthenium and the origin of isotopic anomalies in murchison. *Astrophys. J.* **647**, 1506. https://doi.org/10.1086/505459.

Galoisy L., Pélegrin E., Arrio M. A., Ildefonse P., Calas G., Ghaleb D., Fillet C. and Pacaud F. (1999) Evidence for 6-coordinated zirconium in inactive nuclear waste glasses. *J. Am. Ceram. Soc.* **82**(8), 2219–2224. https://doi.org/10.1111/j.1151-2916.1999.tb02065.x.

Giannozzi P., Baroni S., Bonini N., Calandra M., Car R., Cavazzoni C., Ceresoli D., Chiarotti G. L., Cococcioni M., Dabo I., Corso A. D., de Gironcoli S., Fabris S., Fratesi G., Gebauer R., Gerstmann U., Gougoussis C., Kokalj A., Lazzeri M., Martin-Samos L., Marzari N., Mauri F., Mazzarello R., Paolini S., Pasquarello A., Paulatto L., Sbraccia C., Scandolo S., Sclauzero G., Seitsonen A. P., Smogunov A., Umari P. and Wentzcovitch R. M. (2009) QUANTUM ESPRESSO: a modular and open-source software project for quantum simulations of materials. *J. Phys. Condens. Matter* **21**. https://doi.org/10.1088/0953-8984/21/39/395502 395502.

Greber N. D., Dauphas N., Puchtel I. S., Hofmann B. A. and Arndt N. T. (2017) Titanium stable isotopic variations in chondrites, achondrites and lunar rocks. *Geochim. Cosmochim. Acta* **213**, 534–552. https://doi.org/10.1016/j.gca.2017.06.033.

Guo J. L., Wang Z., Zhang W., Moynier F., Cui D., Hu Z. and Ducea M. N. (2020) Significant Zr isotope variations in single zircon grains recording magma evolution history. *Proc. Natl. Acad. Sci.* **117**(35), 21125–21131. https://doi.org/10.1073/pnas.2002053117.

Harrison T. M. and Watson E. B. (1983) Kinetics of zircon dissolution and zirconium diffusion in granitic melts of variable water content. *Contrib. Mineral. Petrol.* **84**(1), 66–72.

Hart S. R. and Dunn T. (1993) Experimental cpx/melt partitioning of 24 trace elements. *Contrib. Mineral. Petrol.* **113**, 1–8. https://doi.org/10.1007/BF00320827.

Hazen R. M. and Finger L. W. (1979) Crystal structure and compressibility of zircon at high pressure. *Am. Mineral.* **64**, 196–201.

Hiess J., Nutman A. P., Bennett V. C. and Holden P. (2008) Ti-in-zircon thermometry applied to contrasting Archean metamorphic and igneous systems. *Chem. Geol.* **247**, 323–338. https://doi.org/10.1016/j.chemgeo.2007.10.012.

Hohenberg P. and Kohn W. (1964) Inhomogeneous electron gas. *Phys. Rev.* **136**, B864–B871. https://doi.org/10.1103/PhysRev.136.B864.

Howard C. J., Hill R. J. and Reichert B. E. (1988) Structures of ZrO2 polymorphs at room temperature by high-resolution neutron powder diffraction. *Acta Crystallogr. B* **44**, 116–120. https://doi.org/10.1107/S0108768187010279.

Hu J. Y. and Dauphas N. (2017) Double-spike data reduction in the presence of isotopic anomalies. *J. Anal. At. Spectrom.* **32**, 2024–2033. https://doi.org/10.1039/C7JA00187H.

Huang F., Lundstrom C. C. and McDonough W. F. (2006) Effect of melt structure on trace-element partitioning between clinopyroxene and silicic, alkaline, aluminous melts. *Am. Mineral.* **91**, 1385–1400. https://doi.org/10.2138/am.2006.1909.

Ibañez-Mejia M. and Tissot F. L. H. (2019) Extreme Zr stable isotope fractionation during magmatic fractional crystallization. *Sci. Adv.* **5**, eaax8648. https://doi.org/10.1126/sciadv.aax8648.

Inglis E. C., Moynier F., Creech J., Deng Z., Day J. M. D., Teng F.-Z., Bizzarro M., Jackson M. and Savage P. (2019) Isotopic fractionation of zirconium during magmatic differentiation and the stable isotope composition of the silicate Earth. *Geochim. Cosmochim. Acta* **250**, 311–323. https://doi.org/10.1016/j.gca.2019.02.010.

Ishigame M. and Sakurai T. (1977) Temperature dependence of the Raman Spectra of ZrO2. *J. Am. Ceram. Soc.* **60**, 367–369. https://doi.org/10.1111/j.1151-2916.1977.tb15561.x.

Keller C. B., Boehnke P. and Schoene B. (2017) Temporal variation in relative zircon abundance throughout Earth history. *Geochem. Perspect. Lett.*, 179–189. https://doi.org/10.7185/geochemlet.1721.

King, W. H. (1984). Isotope Shifts in Atomic Spectra, Physics of Atoms and Molecules. Springer US. https://doi.org/10.1007/978-1-4899-1786-7.

Kirkpatrick H., Harrison T. M., Liu M., Bell E. A., Ibanez-Mejia M. and Tissot F. (2019) Zr isotope variations in zircon as an indicator of magmatic differentiation. *Presented at the AGU Fall Meeting 2019*. AGU.

Kleinman L. and Bylander D. M. (1982) Efficacious form for model pseudopotentials. *Phys. Rev. Lett.* **48**, 1425–1428. https://doi.org/10.1103/PhysRevLett.48.1425.

Klemme S., Günther D., Hametner K., Prowatke S. and Zack T. (2006) The partitioning of trace elements between ilmenite, ulvospinel, armalcolite and silicate melts with implications for the early differentiation of the moon. *Chem. Geol.* **234**, 251–263. https://doi.org/10.1016/j.chemgeo.2006.05.005.

Knyazev D. A. and Myasoedov N. F. (2001) Specific effects of heavy nuclei in chemical equilibrium. *Sep. Sci. Technol.* **36**, 1677–1696. https://doi.org/10.1081/SS-100104758.

Kohn W. and Sham L. J. (1965) Self-consistent equations including exchange and correlation effects. *Phys. Rev.* **140**, A1133–A1138. https://doi.org/10.1103/PhysRev.140.A1133.

Kolesov B. A., Geiger C. A. and Armbruster T. (2001) The dynamic properties of zircon studied by single-crystal X-ray diffraction and Raman spectroscopy. *Eur. J. Mineral.* **13**, 939–948. https://doi.org/10.1127/0935-1221/2001/0013-0939.

Lazzeri M. and Mauri F. (2003) First-principles calculation of vibrational raman spectra in large systems: signature of small rings in crystalline SiO_2. *Phys. Rev. Lett.* **90**. https://doi.org/10.1103/PhysRevLett.90.036401 036401.

Louvel M., Sanchez-Valle C., Malfait W. J., Testemale D. and Hazemann J.-L. (2013) Zr complexation in high pressure fluids and silicate melts and implications for the mobilization of HFSE in subduction zones. *Geochim. Cosmochim. Acta* **104**, 281–299. https://doi.org/10.1016/j.gca.2012.11.001.

Mavromatis V., Gautier Q., Bosc O. and Schott J. (2013) Kinetics of Mg partition and Mg stable isotope fractionation during its incorporation in calcite. *Geochim. Cosmochim. Acta* **114**, 188–203. https://doi.org/10.1016/j.gca.2013.03.024.

McDonald A. M. (1996) The crystal structure of sabinaite, Na 4Zr2TiO4 (CO3)4. *Can. Mineral.* **34**, 811–815.

Méheut M., Lazzeri M., Balan E. and Mauri F. (2009) Structural control over equilibrium silicon and oxygen isotopic fractionation: a first-principles density-functional theory study. *Chem. Geol. Appl. Non-tradit. Stable Isotopes High-temperature Geochem.* **258**, 28–37. https://doi.org/10.1016/j.chemgeo.2008.06.051.

Méheut M., Lazzeri M., Balan E. and Mauri F. (2007) Equilibrium isotopic fractionation in the kaolinite, quartz, water system: prediction from first-principles density-functional theory. *Geochim. Cosmochim. Acta* **71**, 3170–3181. https://doi.org/10.1016/j.gca.2007.04.012.

Monkhorst H. J. and Pack J. D. (1976) Special points for Brillouin-zone integrations. *Phys. Rev. B* **13**, 5188–5192. https://doi.org/10.1103/PhysRevB.13.5188.

Montorsi M., Leonelli C., Menziani M. C., Du J. and Cormack A. N. (2002) Molecular dynamics study of zirconia containing glasses. *Phys. Chem. Glasses* **43**(4), 137–142.

Morimoto N. (1988) Nomenclature of pyroxenes. *Mineral. Petrol.* **39**, 55–76. https://doi.org/10.1007/BF01226262.

Mungall J. E., Dingwell D. B. and Chaussidon M. (1999) Chemical diffusivities of 18 trace elements in granitoid melts. *Geochim. Cosmochim. Acta* **63**, 2599–2610. https://doi.org/10.1016/S0016-7037(99)00209-4.

Nakamura Y., Fujimaki H., Nakamura N., Tatsumoto M., McKay G. A. and Wagstaff J. (1986) Hf, Zr, and REE partition coefficients between ilmenite and liquid: implications for lunar petrogenesis. *J. Geophys. Res. Solid Earth* **91**, 239–250. https://doi.org/10.1029/JB091iB04p0D239.

Nasdala L., Zhang M., Kempe U., Panczer G., Gaft M., Andrut M. and Plötze M. (2003) Spectroscopic methods applied to zircon. *Rev. Mineral. Geochem.* **53**, 427–467. https://doi.org/10.2113/0530427.

Niederer F. R., Papanastassiou D. A. and Wasserburg G. J. (1985) Absolute isotopic abundances of Ti in meteorites. *Geochim. Cosmochim. Acta* **49**, 835–851. https://doi.org/10.1016/0016-7037(85)90176-0.

Nielsen R. L., Ustunisik G., Weinsteiger A. B., Tepley F. J., Johnston A. D. and Kent A. J. R. (2017) Trace element partitioning between plagioclase and melt: an investigation of the impact of experimental and analytical procedures. *Geochem. Geophys. Geosystems* **18**, 3359–3384. https://doi.org/10.1002/2017GC007080.

Perdew J. P. and Zunger A. (1981) Self-interaction correction to density-functional approximations for many-electron systems. *Phys. Rev. B* **23**, 5048–5079. https://doi.org/10.1103/PhysRevB.23.5048.

Qin T., Wu F., Wu Z. and Huang F. (2016) First-principles calculations of equilibrium fractionation of O and Si isotopes in quartz, albite, anorthite, and zircon. *Contrib. Mineral. Petrol.* **171**, 91. https://doi.org/10.1007/s00410-016-1303-3.

Quintard P. E., Barbéris P., Mirgorodsky A. P. and Merle-Méjean T. (2002) Comparative lattice-dynamical study of the Raman spectra of monoclinic and tetragonal phases of zirconia and hafnia. *J. Am. Ceram. Soc.* **85**, 1745–1749. https://doi.org/10.1111/j.1151-2916.2002.tb00346.x.

Richter F. M., Bruce Watson E., Chaussidon M., Mendybaev R., Christensen J. N. and Qiu L. (2014) Isotope fractionation of Li and K in silicate liquids by Soret diffusion. *Geochim. Cosmochim. Acta* **138**, 136–145. https://doi.org/10.1016/j.gca.2014.04.012.

Richter F. M., Dauphas N. and Teng F.-Z. (2009a) Non-traditional fractionation of non-traditional isotopes: evaporation, chemical diffusion and Soret diffusion. *Chem. Geol. Appl. Non-traditional Stable Isotopes High-temperature Geochem.* **258**, 92–103. https://doi.org/10.1016/j.chemgeo.2008.06.011.

Richter F. M., Davis A. M., DePaolo D. J. and Watson E. B. (2003) Isotope fractionation by chemical diffusion between molten basalt and rhyolite. *Geochim. Cosmochim. Acta* **67**, 3905–3923. https://doi.org/10.1016/S0016-7037(03)00174-1.

Richter F. M., Liang Y. and Davis A. M. (1999) Isotope fractionation by diffusion in molten oxides. *Geochim. Cosmochim. Acta* **63**, 2853–2861. https://doi.org/10.1016/S0016-7037(99)00164-7.

Richter F. M., Watson E. B., Mendybaev R., Dauphas N., Georg B., Watkins J. and Valley J. (2009b) Isotopic fractionation of the major elements of molten basalt by chemical and thermal diffusion. *Geochim. Cosmochim. Acta* **73**, 4250–4263. https://doi.org/10.1016/j.gca.2009.04.011.

Richter F. M., Watson E. B., Mendybaev R. A., Teng F.-Z. and Janney P. E. (2008) Magnesium isotope fractionation in silicate melts by chemical and thermal diffusion. *Geochim. Cosmochim. Acta* **72**, 206–220. https://doi.org/10.1016/j.gca.2007.10.016.

Rignanese G.-M., Detraux F., Gonze X. and Pasquarello A. (2001) First-principles study of dynamical and dielectric properties of tetragonal zirconia. *Phys. Rev. B* **64**. https://doi.org/10.1103/PhysRevB.64.134301 134301.

Robinson K., Gibbs G. V. and Ribbe P. H. (1971) The structure of zircon: a comparison with garnet. *Am. Mineral.* **56**, 782–790.

Roelofsen-Ahl J. N. and Peterson R. C. (1989) Gittinsite; a modification of the thortveitite structure. *Can. Mineral.* **27**, 703–708.

Schauble E. A. (2007) Role of nuclear volume in driving equilibrium stable isotope fractionation of mercury, thallium, and other very heavy elements. *Geochim. Cosmochim. Acta* **9**, 2170–2189. https://doi.org/10.1016/j.gca.2007.02.004.

Schauble E. A. (2004) Applying stable isotope fractionation theory to new systems. *Rev. Mineral. Geochem.* **55**, 65–111. https://doi.org/10.2138/gsrmg.55.1.65.

Schmitt A. K., Danišík M., Evans N. J., Siebel W., Kiemele E., Aydin F. and Harvey J. C. (2011) Acigöl rhyolite field, Central Anatolia (part 1): high-resolution dating of eruption episodes

and zircon growth rates. *Contrib. Mineral. Petrol.* **162**(6), 1215–1231. https://doi.org/10.1007/s00410-011-0648-x.

Smith D. K. and Newkirk W. (1965) The crystal structure of baddeleyite (monoclinic ZrO2) and its relation to the polymorphism of ZrO2. *Acta Crystallographica* **18**(6), 983–991. https://doi.org/10.1107/S0365110X65002402.

Smith D. K. and Newkirk H. W. (1971) Crystal structure of baddeleyite (monoclinic ZrO2) and its relation to the polymorphism of ZrO2. *Acta Crystallogr.* **18**, 983–991.

Smith V. G., Tiller W. A. and Rutter J. W. (1955) A mathematical analysis of solute redistribution during solidification. *Can. J. Phys.* **33**, 723–745. https://doi.org/10.1139/p55-089.

Sokolova E., Hawthorne F. C., Ball N. A., Mitchell R. H. and Ventura G. D. (2006) Vlasovite, Na2 Zr (Si4O11), from the kipawa alkaline complex, Quebec, Canada: crystal-structure refinement and infrared spectroscopy. *Can. Mineral.* **44**, 1349–1356. https://doi.org/10.2113/gscanmin.44.6.1349.

Tian S., Inglis E. C., Creech J. B., Zhang W., Wang Z., Hu Z., Liu Y. and Moynier F. (2020) The zirconium stable isotope compositions of 22 geological reference materials, 4 zircons and 3 standard solutions. *Chem. Geol.* **555**. https://doi.org/10.1016/j.chemgeo.2020.119791 119791.

Tiller W. A., Jackson K. A., Rutter J. W. and Chalmers B. (1953) The redistribution of solute atoms during the solidification of metals. *Acta Metall.* **1**, 428–437. https://doi.org/10.1016/0001-6160(53)90126-6.

Tissot F. L. H. and Dauphas N. (2015) Uranium isotopic compositions of the crust and ocean: age corrections, U budget and global extent of modern anoxia. *Geochim. Cosmochim. Acta* **167**, 113–143. https://doi.org/10.1016/j.gca.2015.06.034.

Tissot F. L. H., Ibañez-Mejia M., Boehnke P., Dauphas N., McGee D., Grove T. L. and Harrison T. M. (2019) 238U/235U measurement in single-zircon crystals: implications for the Hadean environment, magmatic differentiation and geochronology. *J. Anal. At. Spectrom.* **34**, 2035–2052. https://doi.org/10.1039/C9JA00205G.

Tompkins H. G. D., Zieman L. J., Ibañez-Mejia M. and Tissot F. L. H. (2020) Zirconium stable isotope analysis of zircon by MC-ICP-MS: methods and application to evaluating intra-crystalline zonation in a zircon megacryst. *J. Anal. At. Spectrom.*. https://doi.org/10.1039/C9JA00315K.

Troullier N. and Martins J. L. (1991) Efficient pseudopotentials for plane-wave calculations. *Phys. Rev. B* **43**, 1993–2006. https://doi.org/10.1103/PhysRevB.43.1993.

Urey H. C. (1947) The thermodynamic properties of isotopic substances. *J. Chem. Soc. Dalton Trans.*, 562–581.

Valenzano L., Torres F. J., Doll K., Pascale F., Zicovich-Wilson C. M. and Dovesi R. (2006) Ab initio study of the vibrational spectrum and related properties of crystalline compounds; the case of CaCO3 calcite. *Z. Für Phys. Chem.* **220**, 893–912. https://doi.org/10.1524/zpch.2006.220.7.893.

Wang T., Liu X., Sun Y., Lu X. and Wang R. (2020) Coordination of Zr4+/Hf4+/Nb5+/Ta5+ in silicate melts: insight from first principles molecular dynamics simulations. *Chem. Geol.* **555**. https://doi.org/10.1016/j.chemgeo.2020.119814 119814.

Watkins J. M., DePaolo D. J., Huber C. and Ryerson F. J. (2009) Liquid composition-dependence of calcium isotope fractionation during diffusion in molten silicates. *Geochim. Cosmochim. Acta* **73**, 7341–7359. https://doi.org/10.1016/j.gca.2009.09.004.

Watkins J. M., DePaolo D. J., Ryerson F. J. and Peterson B. T. (2011) Influence of liquid structure on diffusive isotope separation in molten silicates and aqueous solutions. *Geochim. Cosmochim. Acta* **75**, 3103–3118. https://doi.org/10.1016/j.gca.2011.03.002.

Watkins J. M., DePaolo D. J. and Watson E. B. (2017) Kinetic fractionation of non-traditional stable isotopes by diffusion and crystal growth reactions. *Rev. Mineral. Geochem.* **82**, 85–125. https://doi.org/10.2138/rmg.2017.82.4.

Watkins J. M., Liang Y., Richter F., Ryerson F. J. and DePaolo D. J. (2014) Diffusion of multi-isotopic chemical species in molten silicates. *Geochim. Cosmochim. Acta* **139**, 313–326. https://doi.org/10.1016/j.gca.2014.04.039.

Watson E. B. (1979) Zircon saturation in felsic liquids: experimental results and applications to trace element geochemistry. *Contrib. Mineral. Petrol.* **70**(4), 407–419. https://doi.org/10.1007/BF00371047.

Watson E. B. (1996) Dissolution, growth and survival of zircons during crustal fusion: kinetic principals, geological models and implications for isotopic inheritance. *Trans. R. Soc. Edinburgh: Earth Sci.* **87**(1–2), 43–56. https://doi.org/10.1017/S0263593300006465.

Watson E. B. and Müller T. (2009) Non-equilibrium isotopic and elemental fractionation during diffusion-controlled crystal growth under static and dynamic conditions. *Chem. Geol. Adv. Exp. Theor. Isotope Geochem.* **267**, 111–124. https://doi.org/10.1016/j.chemgeo.2008.10.036.

Watson E. B. and Ryerson F. J. (1986) Partitioning of zirconium between clinopyroxene and magmatic liquids of intermediate composition. *Geochim. Cosmochim. Acta* **50**, 2523–2526. https://doi.org/10.1016/0016-7037(86)90035-9.

Weyer S., Anbar A. D., Gerdes A., Gordon G. W., Algeo T. J. and Boyle E. A. (2008) Natural fractionation of 238U/235U. *Geochim. Cosmochim. Acta* **72**, 345–359. https://doi.org/10.1016/j.gca.2007.11.012.

Wilke M., Schmidt C., Dubrail J., Appel K., Borchert M., Kvashnina K. and Manning C. E. (2012) Zircon solubility and zirconium complexation in H2O+Na2O+SiO2±Al2O3 fluids at high pressure and temperature. *Earth Planet. Sci. Lett.* **349–350**, 15–25. https://doi.org/10.1016/j.epsl.2012.06.054.

Yang S. and Liu Y. (2016) Nuclear field shift effects on stable isotope fractionation: a review. *Acta Geochim.* **35**, 227–239. https://doi.org/10.1007/s11631-016-0109-3.

Yin Q. Z., Jacobsen S. B., McDonough W. F., Horn I., Petaev M. I. and Zipfel J. (2000) Supernova sources and the 92Nb-92Zr p-process chronometer. *Astrophys. J. Lett.* **536**, L49. https://doi.org/10.1086/312718.

Young E. D., Manning C. E., Schauble E. A., Shahar A., Macris C. A., Lazar C. and Jordan M. (2015) High-temperature equilibrium isotope fractionation of non-traditional stable isotopes: experiments, theory, and applications. *Chem. Geol.* **395**, 176–195. https://doi.org/10.1016/j.chemgeo.2014.12.013.

Zhang H., Liu Y., Zhu K., Siu G., Xiong Y. and Xiong C. (1999) Infrared spectra of nanometre granular zirconia. *J. Phys. Condens. Matter* **11**, 2035–2042. https://doi.org/10.1088/0953-8984/11/8/016.

Zhang W., Wang Z., Moynier F., Inglis E., Tian S., Li M., Liu Y. and Hu Z. (2019) Determination of Zr isotopic ratios in zircons using laser-ablation multiple-collector inductively coupled-plasma mass-spectrometry. *J. Anal. At. Spectrom.* **34**, 1800–1809. https://doi.org/10.1039/C9JA00192A.

Zhao X. and Vanderbilt D. (2002) Phonons and lattice dielectric properties of zirconia. *Phys. Rev. B* **65**. https://doi.org/10.1103/PhysRevB.65.075105 075105.

Associate editor: Mark Rehkamper